Title

Unlocking New Redox Activity in Alluaudite Cathodes through Compositional Design

Journal

Chemistry of Materials, 34(9)

ISSN

0897-4756

Authors

Wu, Vincent C
Giovine, Raynald
Foley, Emily E
et al.

Publication Date

2022-05-10

DOI

10.1021/acs.chemmater.2c00324

Unlocking new redox activity in alluaudite cathodes through compositional design

Vincent C. Wu,[a,c] Raynald Giovine,[a,c] Emily E. Foley,[a,c] Jordan Finzel,[b] Mahalingam Balasubramanian,[d] Elias Sebti,[a,c] Eve M. Mozur,[a,c] Andrew H. Kwon,[c] and Raphaële J. Clément[a,c*]

a. *Materials Department, University of California Santa Barbara, California 93106, United States*
b. *Chemical Engineering Department, University of California Santa Barbara, California 93106, United States*
c. *Materials Research Laboratory, University of California Santa Barbara, California 93106, United States*
d. *Oak Ridge National Laboratory, Oak Ridge, Tennessee 37830, United States*

*E-mail: rclement@ucsb.edu

Abstract

Sodium (Na)-ion conducting polyanionic structures are among the most promising cathode materials to enable more sustainable Na-based battery chemistries to replace current Li-based energy storage systems. Materials adopting the alluaudite structure have been found to reversibly intercalate Na, with phosphate and sulfate derivatives exhibiting moderate to high capacities when used as Na-ion cathodes. However, the development of alluaudite cathodes has been hampered by the fact that largely only $Fe^{2+/3+}$ redox has been observed in this structure. Herein, we show that the $Mn^{2+/3+}$ redox couple can be activated through compositional tuning of alluaudite compounds. Specifically, vanadate compounds were explored to increase the electrical conductivity as compared to the phosphates and sulfates. Al substitution was also employed to buffer the Jahn-Teller distortions of $Mn(III)O_6$ octahedra, further facilitating electron transfer and redox processes. We report the synthesis of a series of new $Na_2Mn_{3-x}Al_x(VO_4)_3$ alluaudite cathodes and employ synchrotron X-ray diffraction, solid-state nuclear magnetic resonance, scanning electron microscopy, density functional theory, X-ray absorption spectroscopy, and magnetometry to characterize the structure, morphology, electronic and magnetic properties of the as-synthesized materials. Electrochemical Na de(intercalation) in $Na_2Mn_{3-x}Al_x(VO_4)_3$ (x = 0, 0.05, 0.2) was probed through galvanostatic cycling, galvanostatic intermittent titration technique, and *ex situ* synchrotron X-ray diffraction. While these materials are all redox active, Al substitution results in a more than two-fold increase in discharge capacity. The successful activation of a higher voltage $Mn^{2+/3+}$ redox couple opens up a new compositional space for alluaudite-type Na-ion cathodes.

Introduction

The development of energy-dense and sustainable batteries is central to meeting the ever-increasing global energy needs. Lithium-ion batteries (LIBs) have enabled the widespread use of portable electronics and are expected to play a major role in the fast-growing electric vehicle industry and in grid-level electrical energy storage, which will require a tremendous increase in lithium (Li) production to match projected demands.[1,2] To reduce the Li consumption-production imbalance,[3,4] 'beyond Li' battery chemistries[5–9] and cost-effective LIB recycling protocols[10–12] are explored. Sodium (Na)-ion batteries are promising candidates to replace the current technology in many application fields and have drawn much research attention over the past few years.[13–19] Notably, Na_2CO_3 and NaCl precursors are much more abundant and easily processable than Li salts, resulting in reduced raw material cost and a more reliable supply chain.[1,20]

Viable Na alternatives to commercial Li systems have proven elusive. A paradigm shift in the development of competitive Na cathodes hinges on the investigation of structures that depart from those explored for Li due to the larger ionic radius, different coordination preference, and lower operating potential of Na compared to Li.[17,20,21] Layered alkali transition metal oxides (A_xMO_2) employed in commercial Li cells suffer from irreversible phase transformations upon complete Na extraction,[17,22,23] which limits their Na (de)intercalation range and capacity.[24–26] Polyanionic compounds consist of a three-dimensional network of $(XO_4)^{n-}$ polyanions (typically, X = Si, P, S, V) and transition metal (MO_6) polyhedra and are amenable to ion intercalation.[2,21,27] Notably, triphylite-[19], maricite-[13], and olivine-type[28] phosphates, NASICON[29]-type phosphates and fluorophosphates[15], as well as pyrophosphates[30] have been identified as Na-ion cathodes.[21] Their covalent frameworks impart high structural stability and prevent lattice oxygen release during (dis)charge.[2,21] Additionally, strongly covalent X-O bonds within the polyanion groups (due to the inductive effect of species X) reduce the covalency of the M-O bonds and stabilize the M-O σ^* orbitals from which electrons are extracted upon oxidation, increasing the operating potential.[31] Seminal work by Goodenough and coworkers[32] has also found a direct link between the inductive effect of the X cation and a narrowing of the M-O conduction band, *i.e.*, reduced electronic conductivity.

While Li-based alluaudite-type compounds are rarely stabilized,[33,34] several Na-containing alluaudites have been reported.[35–39] Their general formula is $A_2M(1)_2M(2)(XO_4)_3$ for X = P, V, and $A_2M(1)M(2)(XO_4)_3$ for X = S, with A = Li, Na. The $A_2M(1)_2M(2)(XO_4)_3$ structure (monoclinic *C*2/*c* space group[40]) is shown in **Figure 1a**. Alluaudites exhibit edge-sharing MO_6 octahedra that form kinked one-dimensional (1D) chains of M(2) octahedral pairs alternating with an M(1) octahedron (**Figure 1b**). The XO_4 tetrahedra (where X = S, P, V) share corners with one another and with MO_6 octahedra, resulting in 1D diffusion tunnels for alkali ions.

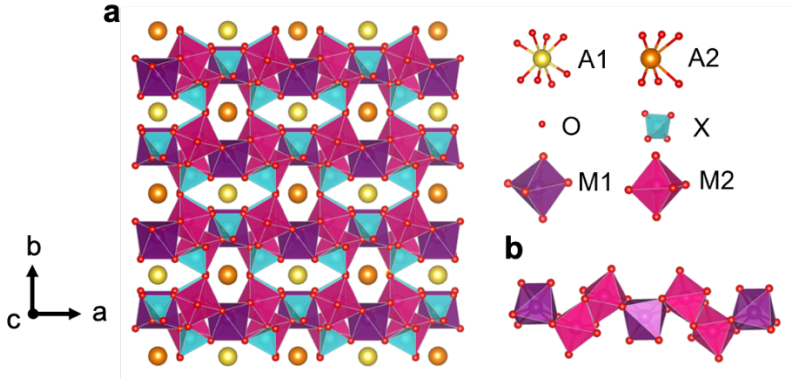

Figure 1. (a) Crystal structure of $A_2M(1)_2M(2)(XO_4)$ (X = P, V) alluaudites and local ion coordinations. (b) Kinked 1D chains of MO_6 octahedra with alternating M1 and M2 sites.

The development of Na-ion alluaudite cathodes has been hindered by the limited number of electrochemically active *M* species in this structure type. Barring just a few compositions,[38,41,42] only Fe^{2+}/Fe^{3+} redox has been harnessed, even in compounds containing multiple *M* species.[35,36,43–48] For instance, $Na_2Fe_{3-x}Mn_x(PO_4)_3$ alluaudites can reach up to 140 mAh/g of reversible capacity for the x = 0 end-member and a steady decrease in capacity is observed as x increases.[36,37,49,50] These cathodes operate at 2.7 V vs. Na/Na^+ and no capacity can be attributed to the higher potential Mn^{2+}/Mn^{3+} couple, leading to rather low energy densities. In contrast, sulfate alluaudites exhibit unprecedently high operating voltages[39] so much so that the potentials of Ni- and Co-based systems fall outside of the electrochemical stability window of typical electrolytes.[51,52] The combination of a highly unstable structure on Na extraction (due to strong repulsion between edge-sharing MO_6 octahedra in the oxidized state) and less negative '-2' charge on the sulfate group compared to the phosphate group results in low capacities for sulfate alluaudites.[39,53,54] Overall, a better understanding of the origin of the electrochemical inertness of Mn, with a redox potential well below the decomposition potential of organic electrolytes even in a sulfate alluaudite, is warranted, and the design of 'beyond Fe' alluaudite cathodes is desirable.

The inactivity of the Mn^{2+}/Mn^{3+} redox couple in alluaudites is thought to stem from the strong Jahn-Teller distortion of $Mn^{3+}O_6$ octahedra, hindering electron hopping between adjacent Mn along the 1D metal chains (**Figure 1b**).[35] To address this, it is anticipated that less covalent polyanion (X-O) bonds that result in broader M-O conduction bands, and the ability to populate empty *d* states near the Fermi level of the X cation, will facilitate electron hopping. We focus here on vanadates as they hold particular promise for 'beyond Fe' alluaudite cathodes due to the presence of more ionic V-O bonds compared to P-O and S-O bonds. Furthermore, V is the only X species with empty *d* states near the Fermi level and studies of Fe-based lithium phosphovanadate compounds have shown that the vanadate moiety increases the electrical conductivity by orders of magnitude.[55–58] Beyond poor electronic conduction, the Jahn-Teller distortion of $Mn^{3+}O_6$ octahedra, compounded by the rigid edge-sharing connectivity of metals along the chains, impedes

oxidation of Mn^{2+} to Mn^{3+}. We speculate that the introduction of Al^{3+}, a main element ion with negligible crystal field stabilization energy, into the 1D metal chains will buffer the strong distortions induced by nearby Mn^{3+} ions and activate Mn redox processes. We note that partial substitution of transition metal species by Al has been found to increase the practical capacity of other polyanionic cathodes, such as fluorophosphates[59,60] although the mechanism by which Al substitution allows a greater amount of Na to be reversibly extracted can vary between structures.

Although several vanadate-based alluaudite structures have been reported to date,[62–67] $Na_2Mn_2Fe(VO_4)_3$ is the only compound that has been electrochemically tested in a Na-ion cell. Its low specific capacity (35 mAh/g) has been accounted for by the redox inactivity of Mn species.[68] Here, we report on the synthesis, structure, and magnetic and electrochemical properties of new $Na_2Mn_3(VO_4)_3$ and Al-substituted $Na_2Mn_{3-x}Al_x(VO_4)_3$ (x = 0.05 and 0.2) alluaudite Na-ion cathodes obtained via a solution-assisted solid-state method. The morphology and crystal and electronic structures of compounds obtained at 300°C and 500°C were examined using a combination of scanning electron microscopy, synchrotron powder X-ray diffraction, solid-state nuclear magnetic resonance, and X-ray absorption spectroscopy. Electrochemical Na de(intercalation) was probed through galvanostatic cycling, the galvanostatic intermittent titration technique, and *ex situ* synchrotron X-ray diffraction. We find the Mn^{2+}/Mn^{3+} couple to be electrochemically active in all $Na_2Mn_{3-x}Al_x(VO_4)_3$ compounds. The incorporation of Al^{3+} ions in the 1D MnO_6 chains leads to a more flexible structure that is able to accommodate the strong distortions induced by the Mn^{3+} ions and facilitates electron hops between Mn species, resulting in an approximately three-fold increase in electronic conductivity and to a greater than two-fold increase in reversible capacity as x is increased from 0 to 0.2. In contrast, $Na_2Mn_{3-x}Al_x(PO_4)_3$ (x = 0, 0.2) cathodes prepared via a similar solution-assisted solid-state method exhibit a low capacity and a small capacity increase upon Al substitution, suggesting that the presence of vanadate polyanions is key to high Mn^{2+}/Mn^{3+} redox activity. Overall, this work demonstrates that a wider compositional space ('beyond Fe') can be opened up for alluaudite cathodes, notably that Mn^{2+}/Mn^{3+} redox can be activated by tuning the local and electronic structure.

Results and Discussion

Average structure and morphology

Alluaudite $Na_2Mn_{3-x}Al_x(VO_4)_3$ (x = 0, 0.05, 0.2) powder samples were synthesized via a solution-assisted, solid-state method (details in the Materials and Methods section) and calcined at 300°C and 500°C for 12 hours. Inductively coupled plasma atomic emission spectroscopy (ICP-AES) characterization was carried out to confirm the composition of the synthesis products. Results are shown in **Table 1** and indicate that the stoichiometries, including the Al content, are close to the targeted ones. It should be noted that the errors listed here only account for uncertainties in the calibration curves and do not include other experimental errors. Thus, a quality control sample was used to estimate the overall experimental error for the estimation of the Na content. The measurements indicate that the practical error for the determination of the Na stoichiometry is ~0.7, which for all materials studied here is within error from the expected value of 2.

	$Na_2Mn_3(VO_4)_3$	$Na_2Mn_{2.95}Al_{0.05}(VO_4)_3$	$Na_2Mn_{2.8}Al_{0.2}(VO_4)_3$
Na	1.93(2)	2.02(2)	1.98(2)
Mn	2.96(1)	2.96(1)	2.84(1)
V	3.00	3.00	3.00
Al	0.010(3)	0.060(2)	0.190(3)

Table 1. Stoichiometries obtained via ICP-AES for $Na_2Mn_{3-x}Al_x(VO_4)_3$, normalized to a V content of 3.00.

Synchrotron powder X-ray diffraction (SXRD) patterns were collected on as-prepared $Na_2Mn_{3-x}Al_x(VO_4)_3$ and refined against the single crystal $Na_2Mn_3(VO_4)_3$ structure reported by Pellizzeri *et al*.[67] As shown in **Figure 2a-d**, the Bragg peaks of all of the samples can be indexed to the monoclinic *C*2/*c* structure, with only a few low intensity impurity peaks, indicating the successful synthesis of vanadate alluaudites with a high phase purity. While the impurity phases could not be indexed, they include diamagnetic Na-containing compounds, as evidenced by ^{23}Na NMR discussed later. Details on Rietveld refinement parameters are shown in **Table S1**.

In the alluaudite structure, Mn occupies two unique octahedral sites, M(1) and M(2), as shown in **Figure 1**. The expected occupancy of M(1) sites by Mn in the 2+ oxidation state, and M(2) sites by a mixture of Mn^{2+} and Mn^{3+} in a 1:1 ratio[40], agrees well with the shorter average bond length for $M(2)O_6$ octahedra. Additionally, the larger Mn-O bond length variation for $M(2)O_6$ octahedra is consistent with the presence of Jahn-Teller distorted Mn^{3+} species with a high spin d^4 electronic configuration.[68] Na occupies two unique sites in the structure, Na(1) and Na(2), which span separate 1D tunnels along the *c* axis and allow for Na diffusion through the structure.

Figures 2a-b show SXRD patterns collected on $Na_2Mn_3(VO_4)_3$ synthesized at 500°C and 300°C, respectively. While the peak positions and their relative intensities are similar for the two samples, indicating that the alluaudite structure is formed at both temperatures, the 500°C sample displays sharper peak shapes, signaling larger domain sizes and/or higher crystallinity. Scanning electron microscopy (SEM) images (**Figure 2e-f**) further indicate that this sample is composed of crystallites with an average size of ~1 μm, while at 300°C, crystallites are an order of magnitude smaller. The same evolution in grain size (**Figure S1**) and SXRD peak width (**Figure S2**) with calcination temperature is observed for $Na_2Mn_{2.8}Al_{0.2}(VO_4)_3$. These results suggest that the particle size of vanadate alluaudites can easily be tuned by varying the calcination temperature.

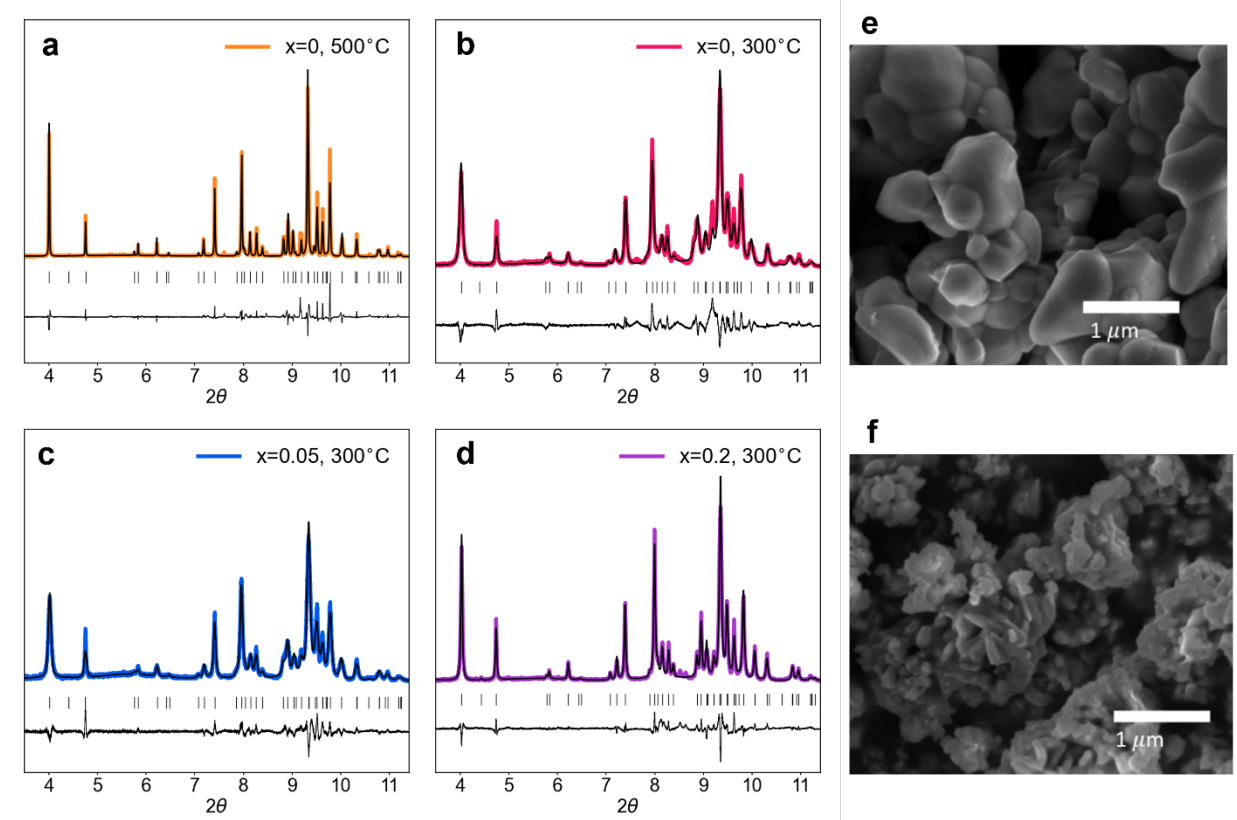

Figure 2. Synchrotron powder XRD patterns collected on a) $Na_2Mn_3(VO_4)_3$ synthesized at 500°C, and b) $Na_2Mn_3(VO_4)_3$, c) $Na_2Mn_{2.95}Al_{0.05}(VO_4)_3$, and d) $Na_2Mn_{2.8}Al_{0.2}(VO_4)_3$ synthesized at 300°C. Rietveld refinements and difference curves are shown in black. SEM images of $Na_2Mn_3(VO_4)_3$ synthesized at e) 500°C and f) 300°C.

Refinements of the SXRD patterns collected on $Na_2Mn_{2.95}Al_{0.05}(VO_4)_3$ and $Na_2Mn_{2.8}Al_{0.2}(VO_4)_3$ synthesized at 300°C are also shown in **Figure 2c-d**. A general decrease in all lattice parameters, but most significantly along the *c* axis, is observed as the Al content increases, leading to an overall decrease in unit cell volume (**Figure S3**). The larger decrease of the *c* lattice parameter relative to the *a* and *b* lattice parameters can be attributed to the complex alluaudite structure, where kinked MO_6 chains in the [101] direction lead to anisotropic lattice changes upon Al substitution. Additionally, the observed anisotropy may indicate that Al incorporation is not a simple substitution; this will be discussed in later sections. Overall, the shrinking of the unit cell as Al is substituted is as expected, due to the replacement of $Mn^{2+/3+}$ ions (0.83 Å – 0.65 Å) by smaller Al^{3+} ions (0.54 Å). Rietveld refinements are unable to resolve whether Al substitutes onto the M(1) or M(2) site, as both models led to similar goodness of fit values. In fact, synchrotron XRD results do not provide unequivocal evidence for Al incorporation into the structure. For this, complementary solid-state NMR (ss-NMR) and X-ray absorption spectroscopy (XAS) were employed to characterize the local structure of the as-prepared samples.

Na local environments in as-synthesized $Na_2Mn_{3-x}Al_x(VO_4)_3$ compounds

Unlike diffraction-based tools, ss-NMR probes the local environments of magnetically-susceptible species in a sample, providing detailed information on short-range atomic arrangements. Here,

^{23}Na spin echo spectra were collected on $Na_2Mn_{3-x}Al_x(VO_4)_3$ alluaudite samples to confirm the presence of two unique Na environments in the structure and reveal potential amorphous and Na-containing impurities that cannot be observed by SXRD. The ^{23}Na spin echo spectra of $Na_2Mn_{3-x}Al_x(VO_4)_3$ (x = 0, 0.05, 0.2) obtained at a magic angle spinning (MAS) speed of 60 kHz and at 7.05 T are shown in **Figure 3a**. These spectra are composed of multiple broad and overlapping signals, making it difficult to identify the isotropic signals corresponding to different Na local environments in the sample. To remedy this, spin echo spectra were recorded at 50 and 60 kHz MAS on all three samples, and the spectra collected on $Na_2Mn_3(VO_4)_3$ are overlaid in **Figure S4**. For a given ^{23}Na NMR signal acquired under MAS, spinning sidebands are separated from the isotropic resonance by multiples of the MAS speed in Hz and their positions are therefore a function of the spinning rate. On the other hand, the isotropic frequency is unaffected by MAS and remains at the same position. Here, two main signals do not shift as the spinning speed is increased from 50 to 60 kHz: one at ~0 ppm, and another one at either ~ −500 ppm or ~ −1200 ppm. The latter resonance is still difficult to locate based on experimental NMR data alone because spinning sidebands from the ~0 ppm resonance overlap with those of the second isotropic signal. To assist spectral assignment, first principles hybrid density functional theory (DFT)/ Hartree Fock (HF) calculations of ^{23}Na NMR parameters were carried out on $Na_2Mn_3(VO_4)_3$ using the CRYSTAL17 software package.

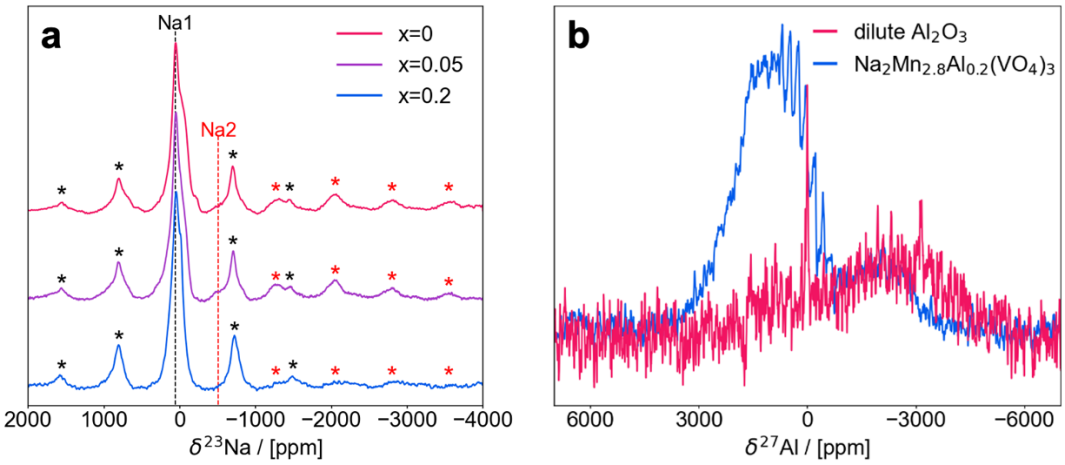

Figure 3. a) ^{23}Na solid-state NMR spin echo spectra collected on $Na_2Mn_{3-x}Al_x(VO_4)_3$ synthesized at 300°C at a MAS speed of 60 kHz and at 7.05 T. Spinning side bands are marked with an asterisk and isotropic peaks with a dotted line. b) ^{27}Al spin echo NMR spectra collected on $Na_2Mn_{2.8}Al_{0.2}(VO_4)_3$ and Al_2O_3 diluted in KBr at a MAS speed of 30 kHz and at 11.7 T.

^{23}Na NMR spectra of $Na_2Mn_{3-x}Al_x(VO_4)_3$ compounds are dominated by paramagnetic interactions between the ^{23}Na nuclear spins and unpaired electron spins from nearby open-shell $Mn^{2+/3+}$ ions. Delocalization of unpaired electron spin density from the Mn 3d orbitals to the Na s orbitals results in an isotropic paramagnetic (Fermi contact) shift (δ_{iso}), while the NMR resonances are broadened by anisotropic interactions between the ^{23}Na nuclear and unpaired electron spin dipole moments. Additionally, ^{23}Na with a nuclear spin S = 3/2 is a quadrupolar nucleus, and interactions between its nuclear quadrupole moment (Q) and the electric field gradient (EFG) cause further broadening of the resonances and a second order quadrupolar shift (δ_Q). The overall ^{23}Na chemical shift δ is thus given by $\delta = \delta_{iso} + \delta_Q$. The experimental ($\delta_{exp}$) and computed ($\delta_{theo}$) shift

values for Na sites in $Na_2Mn_3(VO_4)_3$ are listed in **Table 2**, with full details of the ^{23}Na NMR parameters computed for all three $Na_2Mn_{3-x}Al_x(VO_4)_3$ compositions in **Tables S2-S4** in the SI. Here, δ_{theo} was obtained using two different hybrid exchange-correlation functionals with 20% (B3LYP or H20) and 35% HF exchange (H35), as these have been found to provide upper and lower bounds, respectively, to δ_{exp} for a range of compounds.[69–74] Full expressions for the shifts and additional details on the computational parameters and analysis can be found in the Materials and Methods section and in the SI.

Environment	δ_{exp} / ppm	δ_{theo} / ppm, OPT H20	δ_{theo} / ppm, OPT H35
Na1-a	~60	132	−2
Na1-b	~−40	−10	−122
Na2	~−500	−533	−551

Table 2. ^{23}Na experimental (δ_{exp}) and theoretical (δ_{theo}) shifts obtained for $Na_2Mn_3(VO_4)_3$. The δ_{theo} values were computed using the B3LYP hybrid functional with 20% (H20) and 35% (H35) Hartree-Fock exchange, respectively, as implemented in the CRYSTAL17 code. NMR properties were obtained on ferromagnetically-aligned cells (at 0 K) and subsequently scaled to their paramagnetic values using an experimentally-derived magnetic scaling factor $\Phi = 0.037228$ to compare with the room temperature ^{23}Na NMR shifts (δ_{exp}) obtained at 7.05 T. An experimental sample temperature of T = 323 K was assumed due to frictional heating induced by fast spinning of the NMR rotor during data acquisition.

Our calculations predict that the overall chemical shift of Na1 is in the range of −122 to +133 ppm, while that of Na(2) is in the range of −533 to −551 ppm for $Na_2Mn_3(VO_4)_3$. Hence, we assign the broad ~0 ppm signal to Na in A1 sites and the signal at ~ −550 ppm to Na in A2 sites in the corresponding spectrum in **Figure 3a**. Our calculations further indicate the presence of multiple Na1 environments in this material, denoted as Na1-a and Na1-b in **Table 2**, with slightly different Mn-O-Na interaction geometries and therefore slightly different chemical shifts. The predicted chemical shift difference between these two types of Na1 sites (~110 ppm) is consistent with that between the two shoulders at 60 and −40 ppm in the $Na_2Mn_3(VO_4)_3$ experimental spectrum. Hence, the broad and asymmetric signal at ~0 ppm is attributed to overlapping resonances from Na1-a and Na1-b environments in the alluaudite structure, as well as small amounts of Na-containing diamagnetic impurities with a shift ~0 ppm.

For the $Na_2Mn_{2.95}Al_{0.05}(VO_4)_3$ and $Na_2Mn_{2.8}Al_{0.2}(VO_4)_3$ compositions, a wider range of Na local environments is expected due to partial substitution of paramagnetic Mn ions by diamagnetic Al^{3+} ions. Yet, their ^{23}Na NMR spectra exhibit similar features as for $Na_2Mn_3(VO_4)_3$, with two main resonances at ~0 and ~−500 ppm. The limited number of resolvable isotropic signals is suggestive of fast Na exchange between sites within a given 1D Na diffusion channel (A1 or A2) in the alluaudite structure, giving rise to an average Na(1) resonance at ~0 ppm and to an average Na2 resonance at ~−500 ppm. This interpretation is further supported by the experimentally-observed NMR linewidths that are narrower than the predicted chemical shift separation between the different Na1 and Na2 sites in Al-substituted $Na_2Mn_{3-x}Al_x(VO_4)_3$ (**Tables S3** and **S4**). As the Al content increases, more diamagnetic Na impurities are observed in the region around 0 ppm, as shown in **Figure S5**. Although the relative intensity of this diamagnetic peak is quite small, it nonetheless indicates that not all of the Na is incorporated into the alluaudite structure, particularly

for $Na_2Mn_{2.8}Al_{0.2}(VO_4)_3$. The amount of diamagnetic Na impurities is not easily quantifiable, despite our best attempts to fit the ^{23}Na NMR data and account for differences in signal relaxation rates between the various resonances. We also note that Na-containing diamagnetic impurities typically resonate around 0 ppm and the significant line broadening that results from paramagnetic interactions with Mn from the cathode material leads to strong signal overlap. Hence, it is impossible to identify the impurity phases formed but we believe that Na_2CO_3 and NaOH are likely present.

Confirming Al incorporation into the alluaudite structure

Synchrotron XRD results indicate no significant crystalline impurities formed upon addition of Al precursors to the synthesis of $Na_2Mn_{3-x}Al_x(VO_4)_3$ compounds. Although the decrease in the lattice parameters with increasing Al content provides indirect evidence for the incorporation of Al into the alluaudite structure, the extent of Al incorporation is unclear and amorphous impurity phases such as Al_2O_3 commonly formed at the surface of particles upon solid-state Al reactions cannot be detected via XRD.[75] Thus, ^{27}Al ss-NMR experiments were performed to directly probe the Al environments in the $Na_2Mn_{2.8}Al_{0.2}(VO_4)_3$ sample.

As shown in **Figure 3b** (red spectrum), the formation of a diamagnetic Al_2O_3 impurity phase during synthesis should lead to a narrow ^{27}Al NMR resonance close to 0 ppm. In contrast, Al nuclei in the bulk alluaudite lattice will be in close proximity to $Mn^{2+/3+}$ species, resulting in very broad ^{27}Al NMR resonances with large isotropic paramagnetic shifts (δ_{iso}). Similar to ^{23}Na, ^{27}Al is a quadrupolar nuclei (S = 5/2) and its overall shift δ is given by $\delta = \delta_{iso} + \delta_Q$. The ^{27}Al spectrum collected on $Na_2Mn_{2.8}Al_{0.2}(VO_4)_3$ in **Figure 3b** exhibits a broad resonance at ~1000 ppm. Such a chemical shift is much higher than value reported for ^{27}Al in diamagnetic environments,[76] indicating that most of the Al has been incorporated into the alluaudite crystal structure, where it is in a paramagnetic environment. The experimental ~1000 ppm shift is well within the 872-1266 ppm range of δ_{theo} values predicted using the H20 and H35 hybrid functionals for an alluaudite superstructure where one Mn^{3+} in an Mn(2) site has been replaced by Al^{3+}, with a full set of computed ^{27}Al NMR parameters listed in **Table S5**. A narrow and low intensity signal is observed at 0 ppm, suggesting a small amount of Al_2O_3 diamagnetic impurity in the $Na_2Mn_{2.8}Al_{0.2}(VO_4)_3$ sample. Because the spin echo spectrum was acquired using short interscan delays due to the small amount of Al in the $Na_2Mn_{2.8}Al_{0.2}(VO_4)_3$ sample and low sensitivity of the measurement, the intensity of the slow-relaxing Al_2O_3 signal is truncated. Nonetheless, a semiquantitative fit of the ^{27}Al spectrum obtained on $Na_2Mn_{2.8}Al_{0.2}(VO_4)_3$ provides an upper bound of ~95% for the amount of Al incorporated into the alluaudite structure (**Figure S8**). The broad feature between −500 and −6000 ppm is due to a probe background signal and does not originate from the sample.

To gain further insight into the local structure and oxidation states of Mn species in alluaudite-type $Na_2Mn_{3-x}Al_x(VO_4)_3$ (x = 0, 0.05, 0.2), X-ray absorption spectroscopy (XAS) data were obtained at the Mn K-edge. While the Mn K-edge is highly sensitive to the formal oxidation state of the Mn centers, complex dependencies of the X-ray absorption near edge structure (XANES) spectral features to the local geometry preclude quantitative analysis via linear combination fitting.[77] Nonetheless, the XANES data on all samples is qualitatively consistent with a mixture of Mn^{2+} and Mn^{3+} species, as shown in **Figure 4a**. Additionally, as more Al is substituted into $Na_2Mn_{3-x}Al_x(VO_4)_3$, the XANES edge energy increases, indicating an increase in

the average Mn oxidation state. This trend is further explored through extended x-ray absorption spectroscopy fine structure (EXAFS) analysis. Fourier transformation of the EXAFS data collected on the alluaudite samples reveals clear local structure changes in the R = 1-2 Å range, suggesting an evolution of the geometry of the first coordination shell around Mn upon Al substitution (**Figure 4b**). Fits of the EXAFS data in this range indicate that shorter Mn-O bonds become more prevalent as the Al content is increased. This is evidenced by the increasing number of short Mn-O bonds per Mn center, and by the contraction of the shortest Mn-O bond, upon Al substitution (**Figure 4c**). Fits of the entire R-space and k-space data, along with fitting parameters, are provided in **Figure S9** and **Table S6** in the SI. The decrease in the Mn-O bond length indicates an increase in the average Mn oxidation state as the Al substitution level is increased, in line with the edge energy shift observed in the XANES. These results are surprising given that the average Mn oxidation state is expected to decrease with increasing Al^{3+} content to maintain overall charge neutrality in a phase pure and stoichiometric $Na_2Mn_{3-x}Al_x(VO_4)_3$ sample and indicates an increasing Na deficiency in the $Na_2Mn_{3-x}Al_x(VO_4)_3$ alluaudite phase to maintain charge balance. This is indeed consistent with the presence of an increasing fraction of Na in diamagnetic environments (Na-containing impurity phases) with increasing Al substitution observed by ^{23}Na NMR in **Figure S5**. However, the extent of Mn oxidation upon Al substitution is quite small, as qualitatively there is only a very slight positive shift of the edge energy when going from the x=0 to the x=0.2 sample (**Figure 4a)**. Additionally, from the EXAFS analysis, the average Mn-O bond length only decreases by 0.016 Å in the x=0.2 alluaudite composition, as compared to the x = 0 compound, further indicating that the increase in the average Mn oxidation state and Na deficiency in the substituted alluaudites, and the amount of Na-containing diamagnetic impurities in these samples, are minimal.

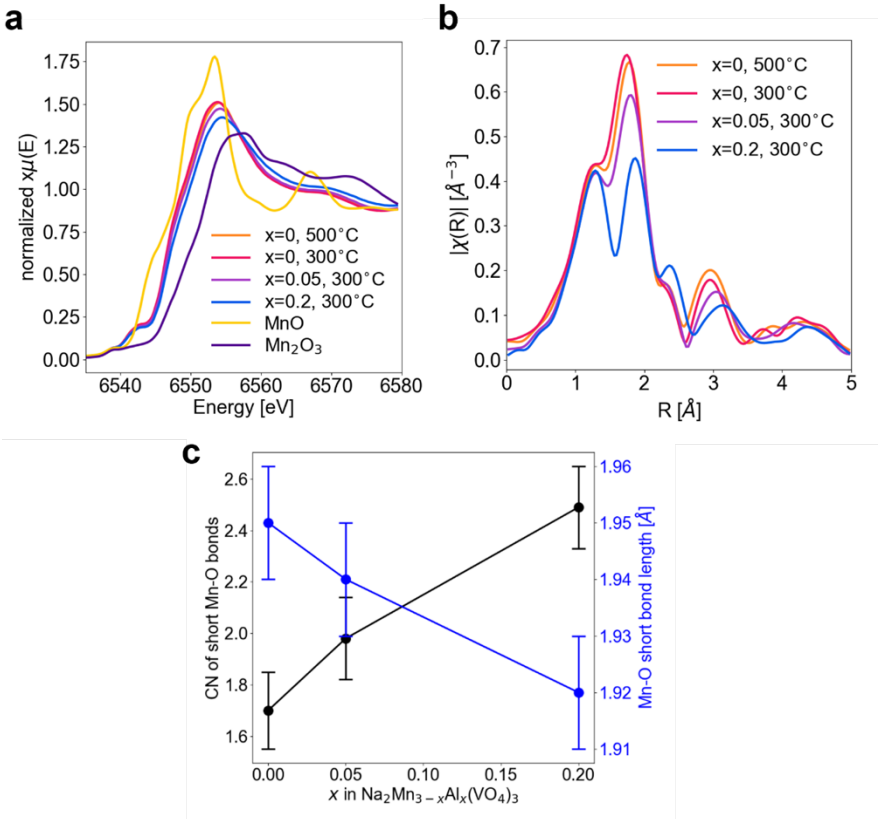

Figure 4. XAS analysis of pristine $Na_2Mn_{3-x}Al_x(VO_4)_3$ compounds synthesized at 300°C, and at 500°C for the x = 0 composition. (a) Normalized XANES spectra, with Mn^{2+} and Mn^{3+} oxide bulk standards. (b) Magnitude of the Fourier transformed EXAFS spectra. (c) Fits of the EXAFS data indicate an increase in the number (CN) of short Mn-O bonds per Mn center, and by the contraction of the shortest Mn-O bond, upon increasing the Al content.

Magnetic properties and electronic conductivity

The magnetic properties of $Na_2Mn_{3-x}Al_x(VO_4)_3$ (x = 0, 0.05, 0.2) synthesized at 300°C were probed with magnetic susceptibility (χ) measurements. The alluaudites behave as Curie-Weiss paramagnets in the high temperature regime, with a magnetic susceptibility of the form $\chi = \frac{C}{T-\Theta}$. Details of the analysis of the inverse magnetic susceptibility ($\frac{1}{\chi}$) versus temperature (T) data shown in **Figure S6** are provided in **Supplementary Note 1**. We note that the magnetic susceptibility data shown in **Figure S6a** comprise signatures of a spin-glass transition for the Al-substituted compounds at 40 K, where a sharp increase in the field-cooled susceptibility is observed below the ordering temperature, that deviates from the zero field-cooled curve. Spin glass behavior is not unexpected since Al replaces Mn and disrupts the ordering of the magnetic moments in these systems. The Curie constant *C*, Weiss constant Θ, and effective magnetic moment μ_{eff}, for the x = 0, 0.05, 0.2 compositions are listed in **Table 3** and reveal that all alluaudites are overall antiferromagnetic (Θ < 0). This result can be rationalized using the Goodenough-Kanamori rules[78–80] that predict the type and magnitude of the (super)exchange interactions between magnetic centers in oxides. In $Na_2Mn_{3-x}Al_x(VO_4)_3$, Mn ions exist as high spin d^4 (Mn^{3+}) and d^5 (Mn^{2+}) octahedral ions, such that both t_{2g} and e_g orbitals contain unpaired electrons and are involved in magnetic couplings. While direct exchange interactions arising from the overlap of *3d* orbitals on adjacent edge-sharing Mn ions ($e_g - e_g$ and $t_{2g} - t_{2g}$ couplings) are always antiferromagnetic, superexchange interactions involving *3d* orbitals on neighboring Mn ions are mediated by oxygen *2p* orbitals and depend on the exact Mn(*3d*)-O(*2p*)-Mn(*3d*) geometry. Here, $e_g - e_g$ and $t_{2g} - t_{2g}$ superexchange interactions occur via a spin polarization mechanism and are expected to be weak and ferromagnetic, while $t_{2g} - e_g$ superexchange take place via spin delocalization and are strong and antiferromagnetic (see **Figure S7** for detailed interaction diagrams). Hence, the overall system is expected to behave as an antiferromagnet, in good agreement with the negative θ values obtained for all three compounds.

x in $Na_2Mn_{3-x}Al_x(VO_4)_3$	Curie constant *C* [emu/Oe/mol]	Weiss constant Θ [K]	μ_{eff} [μ_B]
0	4.91±0.002	−63.2±0.002	6.27
0.05	4.41±0.002	−57.6±0.002	5.94
0.2	3.79±0.001	−50.4±0.001	5.50

Table 3. Magnetic properties of $Na_2Mn_{3-x}Al_x(VO_4)_3$ synthesized at 300°C obtained via a linear regression of the inverse susceptibility (1/χ) versus temperature (T) curves.

A decrease in *C* and μ_{eff} are observed as the Al content x is increased. This trend indicates a reduction in the number of unpaired electron spins per Mn center, *i.e.*, an increase in the average Mn oxidation state, in line with XAS results. The orbital angular momentum of octahedral Mn^{2+} and Jahn-Teller Mn^{3+} ions is effectively quenched and the theoretical magnetic moments of

$Na_2Mn_{3-x}Al_x(VO_4)_3$ compounds can be approximated to their spin only value ($\mu_{SO} \approx 2\sqrt{S(S+1)}\,\mu_B$). For $Na_2Mn_3(VO_4)_3$, there are two high spin Mn^{2+} ions ($3d^5$) and one high spin Mn^{3+} ion ($3d^4$) per formula unit and $\mu_{SO} \approx 5.57\,\mu_B$, which is close to the experimental values shown in **Table 3**. The significant decrease in μ_{eff} as the Al content is increased indicates that Al substitution interferes with the exchange interactions between Mn centers, suggesting that Al^{3+} ions are incorporated into the 1D edge-sharing MnO_6 chains.

The electronic conductivities of $Na_2Mn_{3-x}Al_x(VO_4)_3$ samples synthesized at 300°C were determined through a direct current (DC) polarization method (**Figure S10a, Supplementary Note 3**). The powders were pelletized to similar densities (~60% of the theoretical maximum density) so that the relative conductivities determined through the DC method could be compared. As shown in **Figure S10b**, the electronic conductivity of the alluaudites increases linearly with Al substitution, with an overall approximately three-fold increase in conductivity from the x = 0 to the x = 0.2 compound.

The results shown in this section clearly demonstrate that the magnetic and electronic properties of $Na_2Mn_{3-x}Al_x(VO_4)_3$ alluaudites depend upon the Al substitution level. The increase in the average Mn oxidation state and electronic conductivity of the as-prepared Al-substituted compounds, and the enhanced redox activity of Mn ions in these systems compared to unsubstituted $Na_2Mn_3(VO_4)_3$, can all be accounted for by the presence of Al^{3+} ions in the 1D MnO_6 chains. Since Al^{3+} ions have no crystal field stabilization energy, they can accommodate highly distorted octahedral sites and act to buffer the Mn^{3+}-induced Jahn-Teller distortions along the chains. The 1D MO_6 chains become more flexible upon Al incorporation, such that a greater number of Mn^{3+} ions are stabilized with charge compensating Na vacancies in the as-synthesized Al-substituted compounds. While a lower electronic conductivity might be expected from the presence of insulating AlO_6 octahedra along the 1D MnO_6 chains, these AlO_6 units instead facilitate lattice distortions accompanying electron hops between Mn sites, resulting in more delocalized charge carriers. Additionally, 3D electronic conduction is enabled by the vanadate moieties that link the MnO_6 chains in these systems, as will be evidenced later.

Electrochemical properties

In order to assess their electrochemical performance, $Na_2Mn_{3-x}Al_x(VO_4)_3$ powders were carbon coated and tested in Na-ion half cells at a C/20 rate between 1.5 and 4.0 V vs. Na/Na^+. **Figure S11a** compares the galvanostatic charge-discharge profiles of $Na_2Mn_3(VO_4)_3$ calcined at 300°C and 500°C. The material synthesized at 500°C shows poor electrochemical performance, with very low capacity (~10 mAh/g), while the one synthesized at 300°C displays a reversible capacity of ~35 mAh/g. A similar trend is observed for the Al-substituted compositions (**Figure S11b**). The improved performance of alluaudites calcined at 300°C is most likely due to their smaller primary particle size (**Figure 2b-c**), leading to shorter conduction pathways and more facile extraction/reinsertion of Na^+ ions from/into individual grains. Hence, the results reported hereafter were obtained on alluaudite compounds synthesized at 300°C.

Figure 5a-b shows the galvanostatic charge-discharge curves of $Na_2Mn_{3-x}Al_x(VO_4)_3$ (x = 0, 0.05, and 0.2) cathodes. The open circuit voltage increases from 3.1 V to 3.3 V vs. Na/Na^+ upon Al incorporation, which can be attributed to the higher average Mn oxidation state of the as-

synthesized Al-substituted compounds. Al substitution also leads to a significant increase in reversible capacity, from 35 mAh/g for $Na_2Mn_3(VO_4)_3$, to 60 mAh/g for $Na_2Mn_{2.95}Al_{0.05}(VO_4)_3$, to 75 mAh/g for $Na_2Mn_{2.8}Al_{0.2}(VO_4)_3$. Nonetheless, a large charge-discharge voltage hysteresis is observed for all compositions. For $Na_2Mn_3(VO_4)_3$, the average charge voltage is 3.4 V vs. Na/Na^+, but the average voltage on discharge is only 2.7 V. This hysteresis is exacerbated in the Al-substituted compounds and results from the insertion of additional Na at low potentials (< 2.3 V), bringing down the discharge potential. For $Na_2Mn_{2.8}Al_{0.2}(VO_4)_3$, the average charge voltage remains at 3.4 V vs. Na/Na^+, but the average discharge potential decreases to 2.4 V.

The increased capacity observed upon Al substitution may be surprising given that the average Mn oxidation state in the pristine alluaudite is higher in the x = 0.5 and 0.2 cathodes than in the unsubstituted x = 0 system. However, partial Mn^{2+} oxidation to Mn^{3+} upon Al substitution only reduces the capacity if the limiting factor is the number of redox active Mn^{2+} species in the system (this assumes that all Mn^{2+} present can easily be oxidized to Mn^{3+}). In this case, the theoretical capacity limit would be ~95 mAh/g upon extraction of two Na^+ ions and concurrent oxidation of two Mn^{2+} ions per formula unit. Instead, the capacity of alluaudites is limited by the inability to fully oxidize Mn^{2+} to Jahn-Teller distorted Mn^{3+} due to buildup of lattice strain, which eventually results in a prohibitively high energy barrier, preventing further Mn^{2+} oxidation and limiting the amount of Na that can be extracted on charge. Therefore, although Mn redox is observed in $Na_2Mn_3(VO_4)_3$, its capacity is drastically limited to 35 mAh/g. In the Al-substituted cathodes, the buffering effect of AlO_6 octahedra in the 1D chains results in more facile oxidation of Mn^{2+} to Mn^{3+}. Overall, Al substitution enhances the redox activity of these materials by lowering the energy barrier for $Mn^{2+/3+}$ oxidation and increasing the electronic conductivity.

To better understand the impact of Al substitution on the Na insertion-extraction mechanism in alluaudite cathodes, differential capacity (dQ/dV) curves for $Na_2Mn_3(VO_4)_3$ and $Na_2Mn_{2.8}Al_{0.2}(VO_4)_3$ are compared in **Figure 5c**. Peaks in the dQ/dV plots correspond to discrete electrochemical processes and provide a more sensitive picture of the Na-ion (de)intercalation mechanisms at play than the voltage vs. capacity curves. Both compounds exhibit broad dQ/dV peaks at ~3.4 and ~3.6 V vs. Na/Na^+ on charge and at ~3.3 V on discharge, yet the dQ/dV peaks are more intense for the Al-substituted material, indicating greater redox activity at those potentials. Additional features are observed at 3.68 V on charge and at ~2.4 V on discharge of $Na_2Mn_{2.8}Al_{0.2}(VO_4)_3$, indicating a change in the Na extraction/reinsertion mechanisms upon Al incorporation.

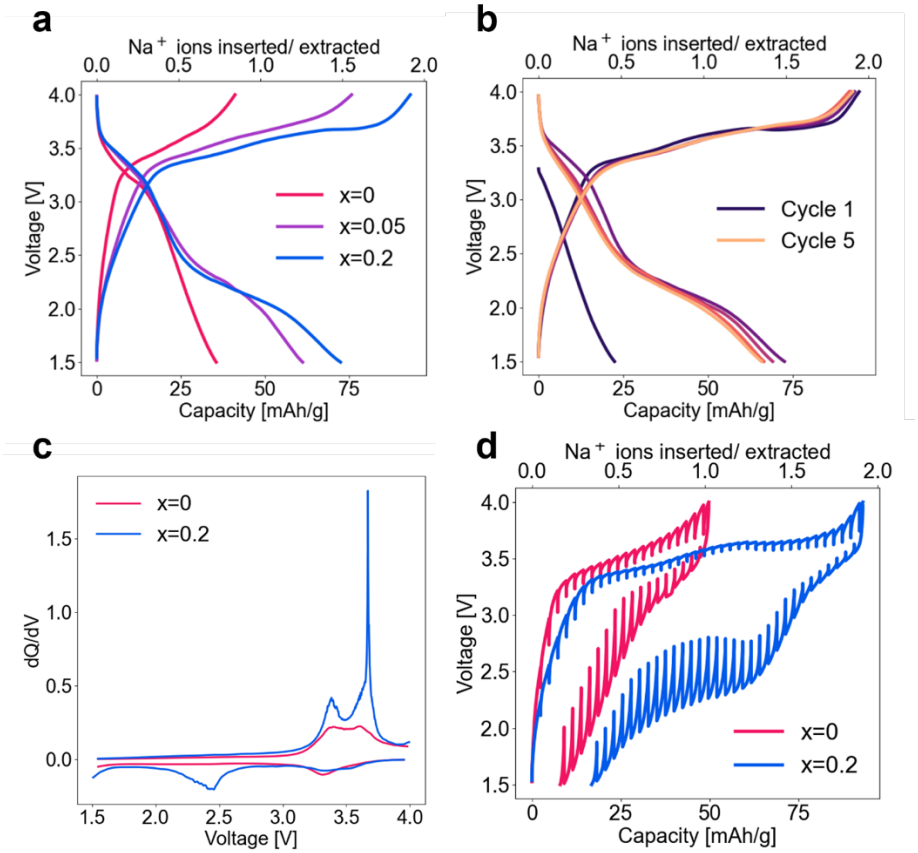

Figure 5. Galvanostatic charge-discharge curves obtained at a C/20 rate for (a) $Na_2Mn_{3-x}Al_x(VO_4)_3$ (x = 0, 0.05, 0.2) during first charge and corresponding discharge process, and for (b) the first five charge-discharge cycles of $Na_2Mn_{2.8}Al_{0.2}(VO_4)_3$. (c) Differential capacity (dQ/dV) and (d) GITT plots of the first charge and corresponding discharge cycle of $Na_2Mn_{3-x}Al_x(VO_4)_3$.

To probe the origin of the abnormally large voltage hysteresis between the charge and discharge processes, and to gain insight into kinetic limitations in $Na_2Mn_3(VO_4)_3$ and $Na_2Mn_{2.8}Al_{0.2}(VO_4)_3$, galvanostatic intermittent titration technique tests were performed on the first charge and corresponding discharge of these materials. After a 30-minute C/20 current pulse, the cell potential was allowed to relax for 2 hours to obtain an approximate equilibrium voltage and the overpotential at various states of charge. As shown in **Figure 5d,** a smaller overpotential is observed on charge for $Na_2Mn_{2.8}Al_{0.2}(VO_4)_3$, especially at voltages > 3.5 V, suggesting that Al incorporation facilitates Na extraction from the alluaudite structure. Generally, larger overpotentials are observed on discharge than on charge, indicating that the reinsertion of Na^+ ions into the alluaudite structure is kinetically hindered. This polarization is particularly severe at voltages below 3.0 V for $Na_2Mn_{2.8}Al_{0.2}(VO_4)_3$ and could imply a change in the Na re-intercalation mechanism at these low potentials. Additionally, a large voltage hysteresis remains even after allowing the cell potential to relax during the GITT process, indicating a thermodynamic asymmetry between the Na extraction and reinsertion processes that is more pronounced for the Al-substituted sample.

Variable cycling rate tests were performed to determine the power capability of $Na_2Mn_{3-x}Al_x(VO_4)_3$ cathodes. As shown in **Figure 6a**, the reversible capacities of the x = 0 and 0.2 cathodes

drop rapidly as the current density increases, signaling kinetically limited diffusion processes at high charge/discharge rates. However, most of the capacity is recovered when the rate is decreased back to C/20, suggesting that the alluaudite structure is mostly unaffected by variable rate cycling. Long-term cycling tests at C/20 (**Figure 6b**) indicate that $Na_2Mn_3(VO_4)_3$, $Na_2Mn_{2.95}Al_{0.05}(VO_4)_3$, and $Na_2Mn_{2.8}Al_{0.2}(VO_4)_3$ retain 81%, 70%, and 75% of their initial discharge capacities after 30 cycles, respectively.

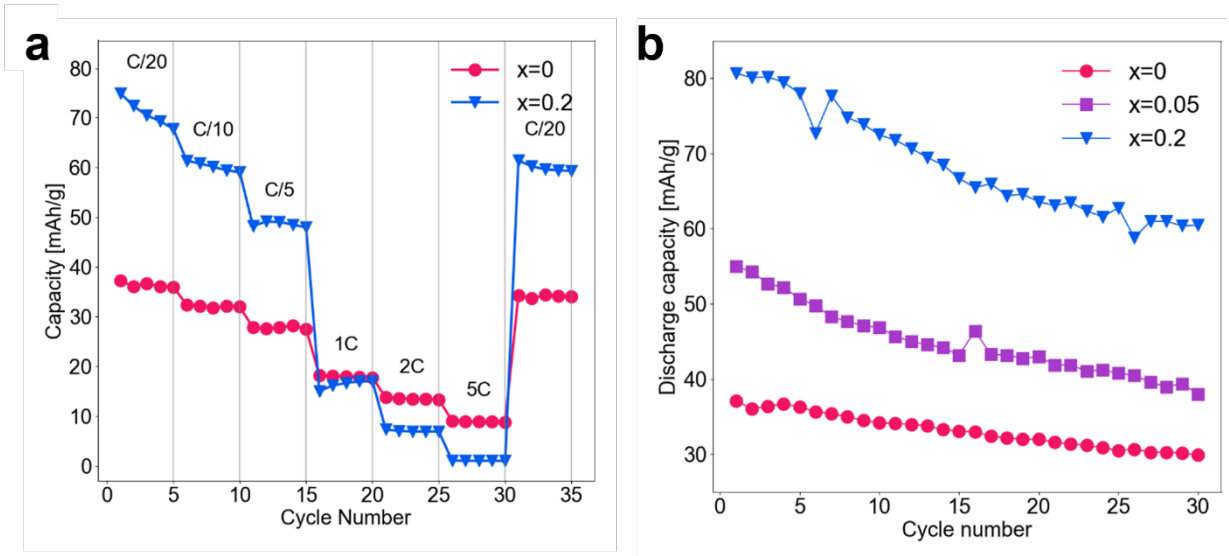

Figure 6. (a) Variable rate cycling tests for $Na_2Mn_3(VO_4)_3$ and $Na_2Mn_{2.8}Al_{0.2}(VO_4)_3$. (b) Discharge capacities for $Na_2Mn_{3-x}Al_x(VO_4)_3$ (x = 0, 0.05 and 0.2) over 30 cycles at a rate of C/20.

Overall, Al substitution for Mn in $Na_2Mn_{3-x}Al_x(VO_4)_3$ cathodes is an effective strategy to activate $Mn^{2+/3+}$ redox processes, with a more than two-fold increase in reversible capacity for the x = 0.2 compound as compared to the unsubstituted material. As mentioned earlier, the increased flexibility of the 1D MO_6 chains upon Al incorporation increases the electronic conductivity and redox activity of the Mn ions, which at least partially accounts for the more facile extraction of Na from the alluaudite structure on charge and increased rate capability. Al substitution also affects the Na (de)intercalation mechanisms, with additional redox processes at ~3.68 V on charge and ~2.4 V on discharge. For the Al-substituted compounds, the additional capacity at low potentials on discharge reduces the operating potential from 2.7 to 2.4 V vs. Na/Na^+ and increases the voltage hysteresis, yet it does not significantly impact the reversibility of the processes over the first 30 cycles.

To assess the effect of the vanadate polyanion on the electrochemical performance of Mn-based alluaudites, phosphate analogues were prepared and electrochemically tested in Na-ion half cells. $Na_2Mn_{3-x}Al_x(PO_4)_3$ (x = 0, 0.2) powder samples were synthesized via a solution-assisted solid-state method similar to the one employed for the vanadates, and their crystallographic data and refined parameters are shown in **Figure S12** and **Table S7**. While the vanadate products are dark brown, the phosphate products are red, indicating a lower electronic conductivity for the latter compounds. Both $Na_2Mn_3(PO_4)_3$ and $Na_2Mn_{2.8}Al_{0.2}(PO_4)_3$ show negligible electrochemical activity (**Figure S13**), underscoring the improvement provided by vanadate polyanions. Thus, the

improvement in electronic conductivity provided by vanadate compounds contributes significantly to the activation of the $Mn^{2+/3+}$ redox couple in alluaudites, alongside Al substitution.

Ex situ synchrotron XRD of cycled samples and effect of Al substitution on the electrochemical processes

To investigate structural changes during sodium (de)intercalation, *ex situ* SXRD patterns were obtained at various states of charge for $Na_2Mn_3(VO_4)_3$ and $Na_2Mn_{2.8}Al_{0.2}(VO_4)_3$ (**Figure 7a-c**). For the x = 0 cathode, a solid solution extraction and reinsertion process is evidenced by the gradual shift in the Bragg peak positions, corresponding to smooth changes in the lattice parameters on charge and discharge (**Figure 7c**). Rietveld refinements of the *ex situ* SXRD patterns reveal a reversible contraction and re-expansion of the alluaudite structure as Na^+ ions are extracted and reintercalated, with changes in the lattice parameters and cell volume presented in **Figure S14**. While the *b* and *c* lattice parameters shrink upon Na^+ extraction, the *a* lattice parameter increases slightly. The overall unit cell volume decreases, as is typical for polyanionic insertion compounds.[49,81,82] As Na^+ ions are reinserted into the structure, the cell volume gradually increases and eventually reverts back to its original value, demonstrating that the $Na_2Mn_3(VO_4)_3$ structure is stable upon cycling, in line with the rather good reversibility observed during galvanostatic cycling. A small volume change of 1.2% is observed on charge, consistent with the limited extraction of only ~0.8 Na^+ ions per formula unit on charge and the rigid polyanionic structure. Site occupancies of the two unique Na sites, Na1 and Na2 were refined and are plotted in **Figure 7d**. The Na occupancy for the 4.0 V *ex situ* point is unreliable as samples collected at the top of charge are particularly unstable, as indicated by the large voltage decay observed after the current flow is stopped (**Figure S15**). From these results, it can be seen that for the unsubstituted alluaudite, only Na^+ ions occupying Na2 sites are extracted on charge, limiting the achievable capacity. This observation is in line with bond valence sum results on the pristine $Na_2Mn_3(VO_4)_3$ structure (**Figure S16**),[83] which predict that migration energy barriers for Na^+ in Na1 sites are high and 0.25 eV higher than those of Na^+ in Na2 sites. Selective Na^+ extraction from Na2 sites has also been observed in the $Na_2Fe_3(PO_4)_3$ and $Na_2Fe_2(SO_4)_3$ alluaudites, via both *ex situ* SXRD and *ab initio* nudged elastic band calculations.[84,85]

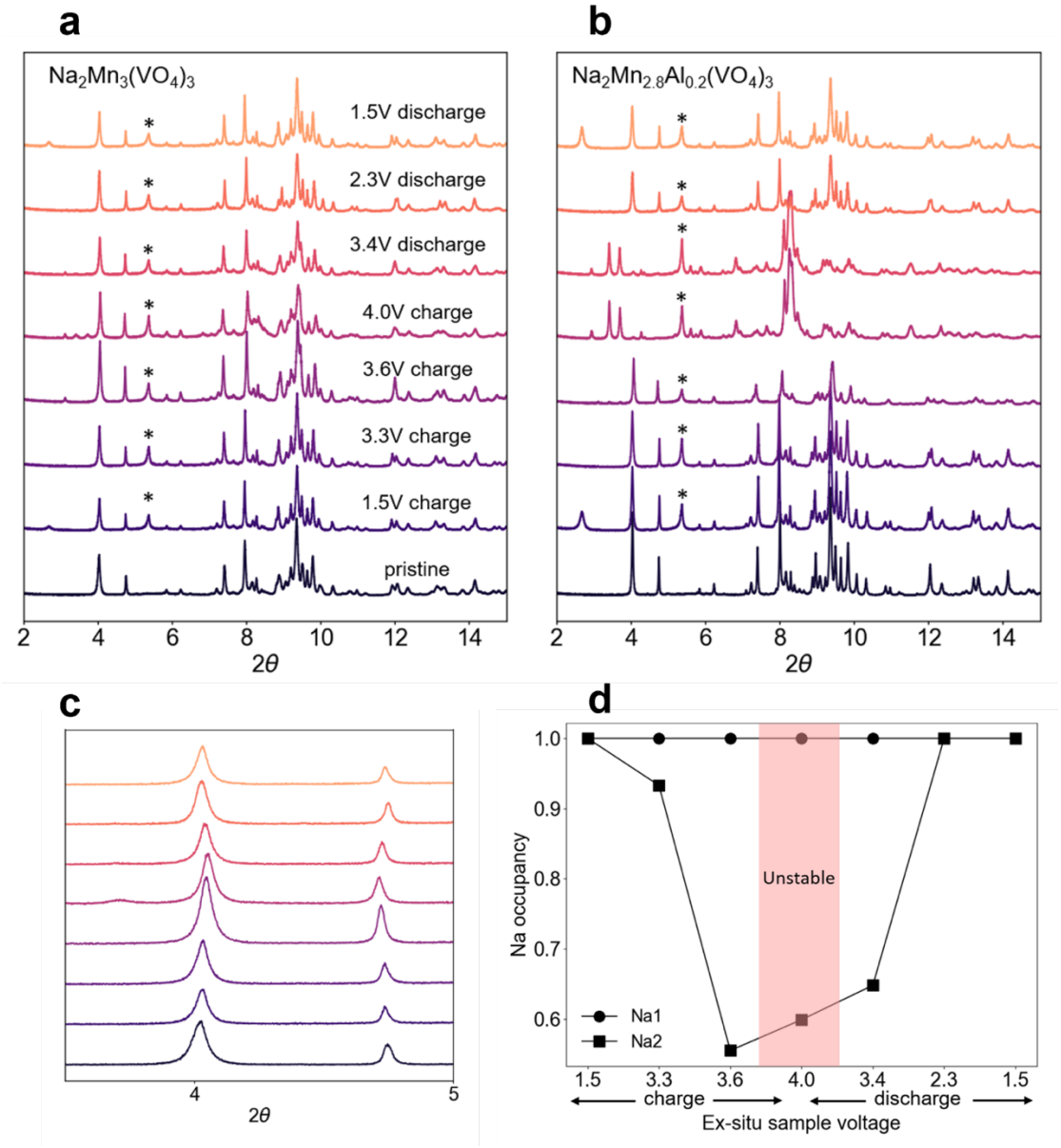

Figure 7. SXRD patterns of *ex situ* alluaudite samples obtained at various points along the first charge and corresponding discharge of the (a) $Na_2Mn_3(VO_4)_3$ and (b) $Na_2Mn_{2.8}Al_{0.2}(VO_4)_3$ cathodes. (c) Enlarged plot of the *ex situ* SXRD patterns collected on the $Na_2Mn_3(VO_4)_3$ cathode, revealing a solid solution behavior on Na (de)intercalation. (d) Evolution of the Na1 and Na2 site occupancies in the $Na_2Mn_3(VO_4)_3$ alluaudite structure on charge and discharge, as obtained from Rietveld refinements of the SXRD data collected on *ex situ* samples. The small impurity phases appearing during cycling are attributed to electrolyte decomposition products and are highlighted with asterisks.

In contrast to $Na_2Mn_3(VO_4)_3$, SXRD spectra collected on *ex situ* $Na_2Mn_{2.8}Al_{0.2}(VO_4)_3$ samples show a clear phase transformation at high voltages. This is first observed in the 4.0 V charged sample, with the appearance of two low-angle peaks around $2\theta = 3.5^\circ$ that signifies the formation of a different structure. In fact, very faint signatures of this new phase can be identified at low angles in the pattern collected on the $Na_2Mn_3(VO_4)_3$ 4.0 V charged sample. This behavior

deviates sharply from phosphate alluaudite variants, where a solid solution reaction is observed even upon extraction of large amounts of Na^+ from the structure.[49] While the alluaudite phase is still present at 4.0 V in $Na_2Mn_{2.8}Al_{0.2}(VO_4)_3$, its phase fraction is heavily reduced at the expense of the new phase. The new phase is difficult to identify yet persists down to at least 3.4 V on discharge. At 2.3 V, the alluaudite phase is completely restored, with no trace of the high voltage phase. Rietveld refinements on *ex situ* $Na_2Mn_{2.8}Al_{0.2}(VO_4)_3$ samples where the alluaudite phase is dominant indicate an increase and decrease in lattice parameters similar to the evolution observed for $Na_2Mn_3(VO_4)_3$ (**Table S8**). Interestingly, the high voltage phase transformation in $Na_2Mn_{2.8}Al_{0.2}(VO_4)_3$ appears to be reversible, based on the similar pristine and discharged SXRD patterns and the stable capacity observed during long-term cycling (**Figure 6b**). One possible cause for this phase transition is Al migration during cycling. While ^{27}Al NMR is, in theory, ideally suited to determine whether Al is extracted from the cathode material on charge, these experiments are prohibitively time-consuming due to the small amount of Al in the cathode materials and the small amount *ex situ* cathode sample that can be prepared for NMR analysis. Although not directly observed, Al substitution enables the extraction of Na^+ from Na1 sites, in addition to Na2 sites, as ~1.5 Na^+ ions are reversibly extracted from the structure. For the x = 0.2 cathode, the asymmetry in the charge-discharge phase transformation observed via *ex situ* SXRD mirrors the results from GITT. Even up to 3.6 V on charge, only the alluaudite phase is observed, however once the phase transition occurs at 4.0 V, it does not revert back to the alluaudite phase until 3.4 V on discharge, which may account for the exacerbated voltage hysteresis and large overpotential observed on discharge (**Figure 5d**). The differences between the Na^+ insertion and extraction mechanisms for the x = 0.2 material implied by GITT are clearly observed in the *ex situ* SXRD patterns and suggest that suppressing the formation of the high voltage phase could increase the efficiency, discharge potential, and energy density of this class of Na-ion cathodes.

Conclusions

The development of Na-ion alluaudite cathodes has been hindered by the limited number of electrochemically active *M* species in this structure type. Barring just a few compositions, only Fe^{2+}/Fe^{3+} redox has been harnessed, even in compounds containing multiple *M* species. Here, we report a series of new alluaudite $Na_2Mn_{3-x}Al_x(VO_4)_3$ (x = 0, 0.05, 0.2) compounds designed to activate the $Mn^{2+/3+}$ redox couple in this family of Na-ion cathodes. The materials were synthesized with a high phase purity via a low-temperature method, and the successful incorporation of Al into the alluaudite structure was confirmed by ^{27}Al solid-state NMR. The increase in the average Mn oxidation state with Al content, as observed by XAS and magnetometry, was accounted for by a small Na deficiency in the as-synthesized Al-substituted compounds, with the presence of a small yet increasing amount of Na-containing diamagnetic impurities observed by ^{23}Na solid-state NMR. The incorporation of Al into the one-dimensional edge-sharing MO_6 chains of the alluaudite structure results in a more flexible framework and buffers the strong Mn^{3+}-induced Jahn-Teller distortions in $Na_2Mn_{3-x}Al_x(VO_4)_3$, allowing for more facile oxidation from Mn^{2+} to Mn^{3+} and additionally resulting in a three-fold increase in electronic conductivity from $Na_2Mn_3(VO_4)_3$ to $Na_2Mn_{2.8}Al_{0.2}(VO_4)_3$. Consequently, Al substitution led to a more than two-fold increase in reversible capacity, from 35 mAh/g to 75 mAh/g. All $Na_2Mn_{3-x}Al_x(VO_4)_3$ compositions exhibited reasonable capacity retention over the first 30 cycles. *Ex situ* synchrotron XRD results revealed that, while Na insertion and extraction occurs via a solid-solution mechanism in $Na_2Mn_3(VO_4)_3$, $Na_2Mn_{2.8}Al_{0.2}(VO_4)_3$ displays a reversible phase transition at high potentials. Overall, both Al

substitution and the presence of vanadate polyanions contribute to the activation of the $Mn^{2+/3+}$ redox couple by increasing the electronic conductivity and by facilitating electron transfer processes in three-dimensions. The successful application of simple compositional design rules to activate a new redox couple in alluaudite cathodes opens up the compositional space for this class of Na-ion positive electrodes.

Materials and Methods

Materials synthesis

$Na_2Mn_{3-x}Al_x(VO_4)_3$ (x = 0, 0.05, and 0.2) compounds were prepared via a solution-assisted solid-state method. Precursor powders of $NaNO_3$, $Mn(C_2H_3O_2)_2.4H_2O$, $Al(NO_3)_3.9H_2O$, and NH_4VO_3 were weighed out in stoichiometric ratios such that the total mass was 1000 mg. Two aqueous solutions were prepared: (1) $NaNO_3$, $Mn(C_2H_3O_2)_2.4H_2O$, and $Al(NO_3)_3.9H_2O$ were dissolved in 5 mL of deionized H_2O, and (2) NH_4VO_3 was dissolved in 15 mL of H_2O under heat. Solutions (1) and (2) were mixed and immediate precipitation of a brown intermediate compound followed. The mixed solution was dried on a hot plate until all moisture had evaporated, leaving a dry powder. The powder was ball milled for 12 hours under 300 rpm to ensure complete mixture of precursors. The resulting ball milled powder was calcined at 300 and 500°C for 12 hours under Ar gas flow.

$Na_2Mn_{3-x}Al_x(PO_4)_3$ (x = 0 and 0.2) compounds were prepared in a similar manner. Precursor powders $NaNO_3$, $Mn(C_2H_3O_2)_2.4H_2O$, $Al(NO_3)_3.9H_2O$, and $NH_4H_2PO_4$ were weighed out in stoichiometric ratios such that the total mass was 1000 mg. Two aqueous solutions were prepared: (1) $NaNO_3$, $Mn(C_2H_3O_2)_2.4H_2O$, and $Al(NO_3)_3.9H_2O$ were dissolved in 5 mL of deionized H_2O, and (2) $NH_4H_2PO_4$ was dissolved in 5 mL of H_2O. Solutions (1) and (2) were mixed, resulting in the precipitation of a light pink intermediate compound. The mixed solution was dried on a hot plate until all moisture had evaporated, leaving a dry powder. The powder was ball milled for 12 hours under 300 rpm, and the resulting powder was calcined at 300°C for the x = 0 composition, and at 500°C for the x = 0.2 composition for 12 hours. Here, phosphate alluaudites were calcined in air, as opposed to their vanadate counterparts prepared under inert conditions. We attribute these differences to the fact that the phosphate group has a stronger inductive effect than the vanadate group, so that Mn ions in the phosphate alluaudite are more difficult to oxidize than in the vanadate. Hence, a more oxidizing environment (ambient air) is needed to form mixed valent $Mn^{2+/3+}$ phosphate alluaudites, while an inert (Ar) environment is required to form the vanadate counterparts.

Powder X-ray diffraction

High-resolution synchrotron powder diffraction patterns for pristine and ex-situ $Na_2Mn_{3-x}Al_x(VO_4)_3$ (x = 0, 0.05, 0.2) compounds synthesized at varying temperatures were collected on Beamline 11-BM at the Advanced Photon Source (APS), Argonne National Laboratory. Room temperature data were collected between 2θ of 0.5° and 50°. Powder X-ray diffraction data for phosphate alluaudites $Na_2Mn_{3-x}Al_x(PO_4)_3$ (x = 0, 0.2) were collected using a laboratory-source Panalytical Empyrean diffractometer with Cu Kα radiation in reflection geometry. All resulting

patterns were refined using the Rietveld method in TOPAS Academic v7.[86] Crystal structures were depicted using VESTA.[87]

Solid-state nuclear magnetic resonance.

^{23}Na ssNMR data were collected at B_0 = 7.05 T (300 MHz for ^{1}H) and room temperature on the pristine alluaudite $Na_2Mn_{3-x}Al_x(VO_4)_3$ (x = 0, 0.05, 0.2) samples synthesized at 300°C using a Bruker super wide-bore NMR spectrometer operating at 79.40 MHz (^{23}Na Larmor frequency) and equipped with an Avance-III console. The data were obtained under magic-angle spinning (MAS) using a 1.3 mm double-resonance HX probe and a spinning frequency ν_R = 60 kHz. ^{23}Na was referenced against a 1 M aqueous solution of sodium chloride (NaCl, $\delta(^{23}Na)$ = 0 ppm). ^{23}Na spin echo spectra were acquired on all samples using a 90° radiofrequency (RF) pulse of 0.74 µs and a 180° RF pulse of 1.48 µs at 200 W. A recycle delay of 35 ms was used, with the value optimized to ensure that the paramagnetic ^{23}Na signal was fully relaxed between pulses.

^{27}Al ss-NMR data were collected on alluaudite $Na_2Mn_{2.8}Al_{0.2}(VO_4)_3$ and α-Al_2O_3 that was diluted with KBr to roughly match the Al weight % expected for the $Na_2Mn_{2.8}Al_{0.2}(VO_4)_3$ sample. Spin-echo spectra were recorded at room temperature and at a B_0 = 11.7 T (500 MHz for ^{1}H) using a Bruker wide-bore NMR spectrometer equipped with an Avance-II console and operating at a frequency of 130.34 MHz. The data were obtained under MAS at a frequency ν_R = 30 kHz using a 2.5 mm double-resonance HX probe. ^{27}Al was referenced against a 1 M aqueous solution of aluminum nitrate ($Al(NO_3)_3$, $\delta(^{27}Al)$ = 0 ppm). ^{27}Al spin echo spectra were acquired on all samples using a 90° radiofrequency (RF) pulse of 0.98 µs and a 180° RF pulse of 1.96 µs at 200 W. A recycle delay of 40 ms was used in order to obtain signal averaged spectra in a reasonable time frame. Solid-state NMR data were processed using the Bruker TopSpin 4.1.1 software and spectra were fitted using the DMfit software.[88] Details on the analysis of the NMR results are provided in the SI.

Magnetometry

Magnetic susceptibility measurements of pristine alluaudite $Na_2Mn_{3-x}Al_x(VO_4)_3$ (x = 0, 0.05, 0.2) samples were measured with a Quantum Design Magnetic Property Measurement System 3 (MPMS) superconducting quantum interference device (SQUID) magnetometer. Powder samples of about 2 mg were packed into a polypropylene holder, snapped into a brass rod, and wrapped with a single layer of Kapton tape. Zero field-cooled (ZFC) and field-cooled (FC) susceptibility data were measured on warming from 2 to 350 K in an applied field of 500 Oe.

X-ray absorption spectroscopy

X-ray absorption spectroscopy (XAS) data were collected on pristine $Na_2Mn_{3-x}Al_x(VO_4)_3$ (x = 0, 0.05, 0.2) samples and MnO, Mn_2O_3, and MnO_2 reference samples at the Advanced Photon Source (APS) on beamline 20-BM using a Si(111) double crystal monochromator. Materials were diluted with hexagonal boron nitride (h-BN) and pressed into self-supporting pellets with an active material loading density of 4-5 mg/cm^2. Mn K-edge (6539 eV) data were collected in transmission mode with ion chambers filled with N_2. A Mn foil was scanned simultaneously for energy calibration. XAS data were processed using the Athena interface and EXAFS fitting used the

Artemis interface of the Demeter package.[89] Details on the EXAFS analysis are provided in the **Supplementary Note 2**.

Electrochemical characterization

The electrochemical performance of alluaudite cathode samples was characterized using Swagelok-type cells assembled in an argon- filled glovebox and using Na metal foil as a combined counter and reference electrode. The alluaudite active material was hand ground with carbon black (Super C65) and polytetrafluoroethylene (PTFE) in a 70:20:10 active:binder:carbon weight ratio. 6.35 mm diameter electrodes films were prepared with a loading density of 4-5 mg/cm^2. Whatman GF/D glass microfiber filters were used as the separator, and a 1M $NaPF_6$ in ethylene carbonate and dimethyl carbonate (EC/ DMC 50/50 v/v) electrolyte was used. Cells were cycled using an Arbin BT2000 potentiostat.

Computational methods

Spin-unrestricted hybrid density functional theory (DFT)/ Hartree Fock (HF) calculations were performed using the CRYSTAL17 all-electron linear combination of atomic orbital code[90,91] to determine ^{23}Na and ^{27}Al NMR parameters in the $Na_2Mn_3(VO_4)_3$ and Al-substituted $Na_2Mn_{3-x}Al_x(VO_4)_3$ structures. Since the Mn(2) site of $Na_2Mn_3(VO_4)_3$ is multivalent with both Mn^{2+} and Mn^{3+}, the initial charge configuration for the starting input structure was obtained from electrostatic energy minimization using an Ewald sum analysis as implemented in Pymatgen[92]. The starting input structure for Al-substituted $Na_2Mn_{3-x}Al_x(VO_4)_3$ was generated by replacing one Mn^{3+} on the Mn(2) site of $Na_2Mn_3(VO_4)_3$ with Al^{3+}. Since there are 12 Mn atoms in the unit cell, this results in a stoichiometry of around $Na_2Mn_{2.92}Al_{0.083}(VO_4)_3$. Two spin-polarized exchange–correlation functionals based upon the B3LYP form,[93–96] and with Fock exchange weights of F_0= 20% (B3LYP or H20) and 35% (H35) were chosen for their good performance for the electronic structure and band gaps of transition metal compounds (B3LYP or H20),[97,98] and for their accurate description of the magnetic properties of related compounds (H35).[99–101] All-electron atom-centered basis sets comprising fixed contractions of Gaussian primitive functions were employed throughout. Two types of basis sets were used for all elements except Al: a smaller basis set (BS-I) was employed for structural optimizations, and a larger basis set (BS-II) was used for computing ^{23}Na and ^{27}Al NMR parameters which require an accurate description of the occupation of core-like electronic states. For Al, a large basis set was used for both structural optimizations and computing NMR parameters. For BS-I, individual atomic sets are of the form (15s7p)/[1s3sp] for Na, (20s12p5d)/ [1s4sp2d] for Mn, (20s12p4d)/ [1s4sp2d] for V, and (14s6p1d)/[1s3sp1d] for O. The values in parentheses denote the number of Gaussian primitives and the values in square brackets the contraction scheme. All BS-I sets were obtained from the CRYSTAL online repository and were unmodified from their previous use in a broad range of compounds.[90] For BS-II, a flexible and extended TZDP-derived (11s7p)/[7s3p] set was used for Na, Ahlrichs DZP-derived sets were used for both Mn (13s9p5d)/[7s5p3d] and V (13s9p5d)/[7s5p3d],[102] and a modified IGLO-III set (14s8p1d)/[5s4p1d] was used for Al. NMR parameters were computed on the fully optimized (atomic positions and cell parameters) $Na_2Mn_{3-x}Al_x(VO_4)_3$ structures. All first principles structural optimizations were carried out in the ferromagnetic (FM) state, after removal of all symmetry constraints (within the P1 space group) and using the H20 and H35 hybrid functionals. A 160 atom 1 x 1 x 2 supercell was used throughout. Anisotropic Monkhorst–Pack

reciprocal space meshes with shrinking factors 3 3 3 were used for both H20 and H35 calculations.[103] Structural optimizations were pursued using the quasi-Newton algorithm with RMS convergence tolerances of 10^{-7}, 0.0003, and 0.0012 a.u. for total energy, root-mean-square (rms) force, and rms displacement, respectively. Tolerances for maximum force and displacement components were set to 1.5 times the respective rms values. Sufficient convergence in total energies and spin densities was obtained by application of integral series truncation thresholds of 10^{-7},10^{-7},10^{-7},10^{-7},and 10^{-14} for Coulomb overlap and penetration, exchange overlap, and g- and n-series exchange penetration, respectively, as defined in the CRYSTAL17 documentation.[90] The final total energies and spin and charge distributions were obtained in the absence of any spin and eigenvalue constraints. NMR parameters were obtained on ferromagnetically aligned supercells.

Acknowledgements

This work made use of the shared facilities of the UC Santa Barbara MRSEC (DMR 1720256), a member of the Materials Research Facilities Network (http://www.mrfn.org) and the computational facilities administered by the Center for Scientific Computing at the CNSI and MRL (an NSF MRSEC; CNS 1725797, DMR 1720256). Use was made of computational facilities purchased with funds from the National Science Foundation (CNS 1725797) and administered by the Center for Scientific Computing (CSC). The CSC is supported by the California NanoSystems Institute and the Materials Research Science and Engineering Center (MRSEC; NSF DMR 1720256) at UC Santa Barbara. Synchrotron diffraction data and X-ray absorption spectroscopy data were collected at beamlines 11-BM and 20-BM, respectively, at the Advanced Photon Source, Argonne National Laboratory, a U.S. Department of Energy (DOE) Office of Science User Facility operated for the DOE Office of Science by Argonne National Laboratory under Contract No. DE-AC02-06CH11357. V. C. Wu, E. E. Foley, J. Finzel and E. Sebti were supported by the NSF Graduate Research Fellowship under Grant No. DGE 1650114. J. Finzel also acknowledges support from the US DOE Office of Graduate Student Research (SCGSR) program administered by the Oak Ridge Institute for Science and Education under contract No. DE-SC0014664. R. J. Clément was supported by an NSF CAREER award under award No. DMR 2141754. This work was partially supported by the RISE internship program through the MRSEC Program of the National Science Foundation under Award No. DMR 1720256. We gratefully acknowledge Sir A. K. Cheetham for the helpful discussions regarding synthesis and diffraction analysis.

Supporting Information Available

Details and errors on Rietveld refinement; XRD patterns on additional samples; SEM images of Al-substituted samples; variable-rate ^{23}Na NMR spin-echo spectra and close-up of ^{23}Na NMR spin-echo spectra; details on comparing first-principles and experimental NMR parameters for ^{23}Na and ^{27}Al; fitting of the ^{27}Al NMR spectrum, magnetic susceptibility measurements and fits; magnetic exchange pathway diagrams; EXAFS fitting procedure and errors; DC polarization method and data; additional electrochemistry for high-temperature vanadates and phosphate alluaudites; voltage decay plots; ex-situ lattice parameter and Na occupancy variations from Rietveld refinement; migration energy barriers from bond-valence sum calculations.

References

(1) Vaalma, C.; Buchholz, D.; Weil, M.; Passerini, S. A Cost and Resource Analysis of Sodium-Ion Batteries. *Nat. Rev. Mater.* **2018**, *3* (4), 1–11.
(2) Ni, Q.; Bai, Y.; Wu, F.; Wu, C. Polyanion-Type Electrode Materials for Sodium-Ion Batteries. *Adv. Sci.* **2017**, *4* (3), 1600275.
(3) Narins, T. P. The Battery Business: Lithium Availability and the Growth of the Global Electric Car Industry. *Extr. Ind. Soc.* **2017**, *4* (2), 321–328.
(4) Olivetti, E. A.; Ceder, G.; Gaustad, G. G.; Fu, X. Lithium-Ion Battery Supply Chain Considerations: Analysis of Potential Bottlenecks in Critical Metals. *Joule* **2017**, *1* (2), 229–243.
(5) Kubota, K.; Dahbi, M.; Hosaka, T.; Kumakura, S.; Komaba, S. Towards K-Ion and Na-Ion Batteries as "Beyond Li-Ion." *Chem. Rec.* **2018**, *18* (4), 459–479.
(6) Muñoz-Torrero, D.; Palma, J.; Marcilla, R.; Ventosa, E. A Critical Perspective on Rechargeable Al-Ion Battery Technology. *Dalt. Trans.* **2019**, *48* (27), 9906–9911.
(7) Zhang, T.; Tang, Y.; Guo, S.; Cao, X.; Pan, A.; Fang, G.; Zhou, J.; Liang, S. Fundamentals and Perspectives in Developing Zinc-Ion Battery Electrolytes: A Comprehensive Review. *Energy Environ. Sci.* **2020**, *13* (12), 4625–4665.
(8) Yoo, H. D.; Shterenberg, I.; Gofer, Y.; Gershinsky, G.; Pour, N.; Aurbach, D. Mg Rechargeable Batteries: An on-Going Challenge. *Energy Environ. Sci.* **2013**, *6* (8), 2265–2279.
(9) Tapia-Ruiz, N.; Armstrong, A. R.; Alptekin, H.; Amores, M. A.; Au, H.; Barker, J.; Boston, R.; Brant, W. R.; Brittain, J. M.; Chen, Y.; Chhowalla, M.; Choi, Y. S.; Costa, S. I. R.; Ribadeneyra, M. C.; Cussen, S. A.; Cussen, E. J.; David, W. I. F.; Desai, A. V.; Dickson, S. A. M.; Eweka, E. I.; Forero-Saboya, J. D.; Grey, C. P.; Griffin, J. M.; Gross, P.; Hua, X.; Irvine, J. T. S.; Johansson, P.; Jones, M. O.; Karlsmo, M.; Kendrick, E.; Kim, E.; Kolosov, O. V.; Li, Z.; Mertens, S. F. L.; Mogensen, R.; Monconduit, L.; Morris, R. E.; Naylor, A. J.; Nikman, S.; O'Keefe, C. A.; Ould, D. M. C.; Palgrave, R. G.; Poizot, P.; Ponrouch, A.; Renault, S.; Reynolds, E. M.; Rudola, A.; Sayers, R.; Scanlon, D. O.; Sen, S.; Seymour, V. R.; Silván, B.; Sougrati, M. T.; Stievano, L.; Stone, G. S.; Thomas, C. I.; Titirici, M. M.; Tong, J.; Wood, T. J.; Wright, D. S.; Younesi, R. 2021 Roadmap for Sodium-Ion Batteries. *J. Phys. Energy* **2021**, *3* (3), 031503.
(10) Gaines, L.; Dai, Q.; Vaughey, J. T.; Gillard, S. Direct Recycling R&D at the ReCell Center. *Recycling* **2021**, *6* (2), 31.
(11) Tan, D. H. S.; Xu, P.; Yang, H.; Kim, M.; Nguyen, H.; Wu, E. A.; Doux, J.-M.; Banerjee, A.; Meng, Y. S.; Chen, Z. Sustainable Design of Fully Recyclable All Solid-State Batteries. *MRS Energy Sustain.* **2020**, *7* (1), E23.
(12) Xu, P.; Dai, Q.; Gao, H.; Liu, H.; Zhang, M.; Li, M.; Chen, Y.; An, K.; Meng, Y. S.; Liu, P.; Li, Y.; Spangenberger, J. S.; Gaines, L.; Lu, J.; Chen, Z. Efficient Direct Recycling of Lithium-Ion Battery Cathodes by Targeted Healing. *Joule* **2020**, *4* (12), 2609–2626.
(13) Kim, J.; Seo, D.-H.; Kim, H.; Park, I.; Yoo, J.-K.; Jung, S.-K.; Park, Y.-U.; Goddard III, W. A.; Kang, K. Unexpected Discovery of Low-Cost Maricite NaFePO 4 as a High-Performance Electrode for Na-Ion Batteries. *Energy Environ. Sci.* **2015**, *8* (2), 540–545.
(14) Adamczyk, E.; Pralong, V. Na2Mn3O7: A Suitable Electrode Material for Na-Ion Batteries? *Chem. Mater.* **2017**, *29* (11), 4645–4648.
(15) Jiang, T.; Chen, G.; Li, A.; Wang, C.; Wei, Y. Sol–Gel Preparation and Electrochemical Properties of Na3V2(PO4)2F3/C Composite Cathode Material for Lithium Ion Batteries.

J. Alloys Compd. **2009**, *478* (1–2), 604–607.
(16) Su, D.; Wang, C.; Ahn, H. J.; Wang, G. Single Crystalline Na0.7MnO2 Nanoplates as Cathode Materials for Sodium-Ion Batteries with Enhanced Performance. *Chem. - A Eur. J.* **2013**, *19* (33), 10884–10889.
(17) Clément, R. J.; Bruce, P. G.; Grey, C. P. Review — Manganese-Based P2-Type Transition Metal Oxides as Sodium-Ion Battery Cathode Materials. *J. Electrochem. Soc.* **2015**, *162* (14), A2589.
(18) Lee, J.; Kitchaev, D. A.; Kwon, D. H.; Lee, C. W.; Papp, J. K.; Liu, Y. S.; Lun, Z.; Clément, R. J.; Shi, T.; McCloskey, B. D.; Guo, J.; Balasubramanian, M.; Ceder, G. Reversible Mn2+/Mn4+ Double Redox in Lithium-Excess Cathode Materials. *Nature* **2018**, *556* (7700), 185–190.
(19) Zhu, Y.; Xu, Y.; Liu, Y.; Luo, C.; Wang, C. Comparison of Electrochemical Performances of Olivine NaFePO 4 in Sodium-Ion Batteries and Olivine LiFePO 4 in Lithium-Ion Batteries. *Nanoscale* **2012**, *5* (2), 780–787.
(20) Kaufman, J. L.; Vinckeviči, J.; Kolli, S. K.; Goiri, J. G.; Van der Ven, A. Understanding Intercalation Compounds for Sodium-Ion Batteries and Beyond. *Philos. Trans. R. Soc. A* **2019**, *377* (2152), 20190020.
(21) Masquelier, C.; Croguennec, L. Polyanionic (Phosphates , Silicates , Sulfates) Frameworks as Electrode Materials for Rechargeable Li (or Na) Batteries. *Chem. Rev.* **2013**, *113* (8), 6552–6591.
(22) Yabuuchi, N.; Yoshida, H.; Komaba, S. Crystal Structures and Electrode Performance of Alpha-NaFeO2 for Rechargeable Sodium Batteries. *Electrochemistry* **2012**, *80* (10), 716–719.
(23) Lee, D. H.; Xu, J.; Meng, Y. S. An Advanced Cathode for Na-Ion Batteries with High Rate and Excellent Structural Stability. *Phys. Chem. Chem. Phys.* **2013**, *15* (9), 3304–3312.
(24) Guignard, M.; Didier, C.; Darriet, J.; Bordet, P.; Elkaïm, E.; Delmas, C. P2-NaxVO2 System as Electrodes for Batteries and Electron-Correlated Materials. *Nat. Mater. 2012 121* **2012**, *12* (1), 74–80.
(25) Berthelot, R.; Carlier, D.; Delmas, C. Electrochemical Investigation of the P2–NaxCoO2 Phase Diagram. *Nat. Mater. 2010 101* **2010**, *10* (1), 74–80.
(26) Delmas, C.; Braconnier, J. J.; Fouassier, C.; Hagenmuller, P. Electrochemical Intercalation of Sodium in NaxCoO2 Bronzes. *Solid State Ionics* **1981**, *3–4* (C), 165–169.
(27) Masquelier, C.; Padhi, A. K.; Nanjundaswamy, K. S.; Goodenough, J. B. New Cathode Materials for Rechargeable Lithium Batteries: The 3-D Framework Structures Li3Fe2(XO4)3(X=P, As). *J. Solid State Chem.* **1998**, *135* (2), 228–234.
(28) Moreau, P.; Guyomard, D.; Gaubicher, J.; Boucher, F. Structure and Stability of Sodium Intercalated Phases in Olivine FePO 4. *Chem. Mater* **2010**, *22*, 4126–4128.
(29) Jian, Z.; Zhao, L.; Pan, H.; Hu, Y. S.; Li, H.; Chen, W.; Chen, L. Carbon Coated Na3V2(PO4)3 as Novel Electrode Material for Sodium Ion Batteries. *Electrochem. commun.* **2012**, *14* (1), 86–89.
(30) Kim, H.; Shakoor, R. A.; Park, C.; Lim, S. Y.; Kim, J.-S.; Jo, Y. N.; Cho, W.; Miyasaka, K.; Kahraman, R.; Jung, Y.; Choi, J. W. Na2FeP2O7 as a Promising Iron-Based Pyrophosphate Cathode for Sodium Rechargeable Batteries: A Combined Experimental and Theoretical Study. *Adv. Funct. Mater.* **2013**, *23* (9), 1147–1155.
(31) Gutierrez, A.; Benedek, N. A.; Manthiram, A. Crystal-Chemical Guide for Understanding

Redox Energy Variations of M 2+/3+ Couples in Polyanion Cathodes for Lithium-Ion Batteries. *Chem. Mater.* **2013**, *25* (20), 4010–4016.
(32) Padhi, A. K.; Nanjundaswamy, K. S.; Masquelier, C.; Okada, S.; Goodenough, J. B. Effect of Structure on the Fe3 + / Fe2 + Redox Couple in Iron Phosphates. *J. Electrochem. Soc.* **1997**, *144* (5), 1609–1613.
(33) Trad, K.; Castets, A.; Wattiaux, A.; Delmas, C.; Ben Amara, M.; Carlier, D. Li0.75Mn1.50Fe1.75(PO4)3: First Alluaudite-Type Iron Phosphate Containing Only Li+ as Alkaline Ions. *J. Solid State Chem.* **2018**, *265*, 12–17.
(34) Kim, J.; Kim, H.; Park, I.; Park, Y. U.; Yoo, J. K.; Park, K. Y.; Lee, S.; Kang, K. LiFePO4 with an Alluaudite Crystal Structure for Lithium Ion Batteries. *Energy Environ. Sci.* **2013**, *6* (3), 830–834.
(35) Trad, K.; Carlier, D.; Croguennec, L.; Wattiaux, A.; Ben Amara, M.; Delmas, C. NaMnFe2(PO4)3 Alluaudite Phase: Synthesis, Structure, and Electrochemical Properties as Positive Electrode in Lithium and Sodium Batteries. *Chem. Mater.* **2010**, *22* (19), 5554–5562.
(36) Huang, W.; Li, B.; Saleem, M. F.; Wu, X.; Li, J.; Lin, J.; Xia, D.; Chu, W.; Wu, Z. Self-Assembled Alluaudite Na2Fe3-XMnx(PO4)3 Micro/ Nanocompounds for Sodium-Ion Battery Electrodes: A New Insight into Their Electronic and Geometric Structure. *Chem. - A Eur. J.* **2015**, *21* (2), 851–860.
(37) Liu, D.; Palmore, G. T. R. Synthesis, Crystal Structure, and Electrochemical Properties of Alluaudite Na1.702Fe3(PO4)3 as a Sodium-Ion Battery Cathode. *ACS Sustain. Chem. Eng.* **2017**, *5* (7), 5766–5771.
(38) Kim, J.; Kim, H.; Lee, S.; Myung, S. T. Development of a New Alluaudite-Based Cathode Material with High Power and Long Cyclability for Application in Na Ion Batteries in Real-Life. *J. Mater. Chem. A* **2017**, *5* (42), 22334–22340.
(39) Barpanda, P.; Oyama, G.; Nishimura, S.; Chung, S. C.; Yamada, A. A 3.8-V Earth-Abundant Sodium Battery Electrode. *Nat. Commun.* **2014**, *5* (1), 1–8.
(40) Dwibedi, D.; Barpanda, P.; Yamada, A. Alluaudite Battery Cathodes. *Small Methods* **2020**, *4* (7), 1–18.
(41) Kim, J.; Kim, H.; Park, K. Y.; Park, Y. U.; Lee, S.; Kwon, H. S.; Yoo, H. I.; Kang, K. Alluaudite LiMnPO4: A New Mn-Based Positive Electrode for Li Rechargeable Batteries. *J. Mater. Chem. A* **2014**, *2* (23), 8632–8636.
(42) Zhang, P.; Yang, K.; Song, L.; Feng, H. J.; Gao, J. An Alluaudite-Type Sodium-Ion Battery Cathode Candidate Na2Mn2V(PO4)3: Crystal Growth, Preparation, Structure and Electrochemical Properties. *J. Alloys Compd.* **2019**, *783*, 409–415.
(43) Dwibedi, D.; Gond, R.; Barpanda, P. Alluaudite NaCoFe2(PO4)3 as a 2.9 v Cathode for Sodium-Ion Batteries Exhibiting Bifunctional Electrocatalytic Activity. *Chem. Mater.* **2019**, *31* (18), 7501–7509.
(44) R. Essehli; I. Belharouak; Yahia, H. Ben; K. Maher; A. Abouimrane; B. Orayech; S. Calder; Zhou, X. L.; Z. Zhou; Y-K. Sun. Alluaudite Na 2 Co 2 Fe(PO 4) 3 as an Electroactive Material for Sodium Ion Batteries. *Dalt. Trans.* **2015**, *44* (17), 7881–7886.
(45) Trad, K.; Carlier, D.; Croguennec, L.; Wattiaux, A.; Ben Amara, M.; Delmas, C. Structural Study of the Li0.5Na0.5MnFe 2(PO4)3and Li0.75Na 0.25MnFe2(PO4)3alluaudite Phases and Their Electrochemical Properties as Positive Electrodes in Lithium Batteries. *Inorg. Chem.* **2010**, *49* (22), 10378–10389.
(46) Wang, X.; Zhang, H.; Xu, Y.; Chen, C.; Yuan, H.; Wang, Y. CTAB-Assisted Multiwalled

Carbon Nanotube-Loaded NaFe2Mn(PO4)3 Materials as High Performance Cathodes for Sodium-Ion Batteries. *RSC Adv.* **2016**, *6* (72), 67986–67991.
(47) Essehli, R.; Belharouak, I.; Ben Yahia, H.; Chamoun, R.; Orayech, B.; El Bali, B.; Bouziane, K.; Zhou, X. L.; Zhou, Z. α-Na2Ni2Fe(PO4)3: A Dual Positive/Negative Electrode Material for Sodium Ion Batteries. *Dalt. Trans.* **2015**, *44* (10), 4526–4532.
(48) Harbaoui, D.; Sanad, M. M. S.; Rossignol, C.; Hlil, E. K.; Amdouni, N.; Zaidat, K.; Obbade, S. Effect of Divalent Transition Metal Ions on Physical, Morphological, Electrical and Electrochemical Properties of Alluaudite Phases Na2M2+2Fe3+(PO4)3 (M = Mn, Co and Ni): Cathode Materials for Sodium-Ions Batteries. *J. Alloys Compd.* **2022**, *901*, 163641.
(49) Essehli, R.; Ben Yahia, H.; Maher, K.; Sougrati, M. T.; Abouimrane, A.; Park, J. B.; Sun, Y. K.; Al-Maadeed, M. A.; Belharouak, I. Unveiling the Sodium Intercalation Properties in Na1.86□0.14Fe3(PO4)3. *J. Power Sources* **2016**, *324*, 657–664.
(50) Dwibedi, D.; Jaschin, P. W.; Gond, R.; Barpanda, P. Revisiting the Alluaudite NaMnFe2(PO4)3 Sodium Insertion Material: Structural, Diffusional and Electrochemical Insights. *Electrochim. Acta* **2018**, *283*, 850–857.
(51) Araujo, R. B.; Chakraborty, S.; Barpanda, P.; Ahuja, R. Na2M2(SO4)3 (M = Fe, Mn, Co and Ni): Towards High-Voltage Sodium Battery Applications. *Phys. Chem. Chem. Phys.* **2016**, *18* (14), 9658–9665.
(52) Dwibedi, D.; Gond, R.; Dayamani, A.; Araujo, R. B.; Chakraborty, S.; Ahuja, R.; Barpanda, P. Na2.32Co1.84(SO4)3 as a New Member of the Alluaudite Family of High-Voltage Sodium Battery Cathodes. *Dalt. Trans.* **2017**, *46* (1), 55–63.
(53) Oyama, G.; Nishimura, S.; Suzuki, Y.; Okubo, M.; Yamada, A. Off-Stoichiometry in Alluaudite-Type Sodium Iron Sulfate Na2+2xFe2-x(SO4)3 as an Advanced Sodium Battery Cathode Material. *ChemElectroChem* **2015**, *2* (7), 1019–1023.
(54) Ming, J.; Barpanda, P.; Nishimura, S. I.; Okubo, M.; Yamada, A. An Alluaudite Na2 + 2xFe2 - X(SO4)3(x = 0.2) Derivative Phase as Insertion Host for Lithium Battery. *Electrochem. commun.* **2015**, *51*, 19–22.
(55) Garbarczyk, J. E.; Wasiucionek, M.; MacHowski, P.; Jakubowski, W. Transition from Ionic to Electronic Conduction in Silver–Vanadate–Phosphate Glasses. *Solid State Ionics* **1999**, *119* (1–4), 9–14.
(56) Garbarczyk, J. E.; Pietrzak, T. K.; Wasiucionek, M.; Kaleta, A.; Dorau, A.; Nowiński, J. L. High Electronic Conductivity in Nanostructured Materials Based on Lithium-Iron-Vanadate-Phosphate Glasses. *Solid State Ionics* **2015**, *272*, 53–59.
(57) Hadouchi, M.; Assani, A.; Saadi, M.; El Ammari, L. The Alluaudite-Type Crystal Structures of Na2(Fe/Co)2Co(VO4)3 and Ag2(Fe/Co)2Co(VO4)3. *Acta Crystallogr. Sect. E Crystallogr. Commun.* **2016**, *72*, 1017–1020.
(58) Clemens, O.; Bauer, M.; Haberkorn, R.; Springborg, M.; Beck, H. P. Synthesis and Characterization of Vanadium-Doped LiMnPO 4-Compounds: LiMn(PO 4) x (VO 4) 1−x (0.8 ≤ x ≤ 1.0). *Chem. Mater.* **2012**, *24* (24), 4717–4724.
(59) Bianchini, M.; Xiao, P.; Wang, Y.; Ceder, G.; Bianchini, M.; Xiao, P.; Ceder, G.; Wang, Y. Additional Sodium Insertion into Polyanionic Cathodes for Higher-Energy Na-Ion Batteries. *Adv. Energy Mater.* **2017**, *7* (18), 1700514.
(60) Olchowka, J.; Nguyen, L. H. B.; Broux, T.; Sanz Camacho, P.; Petit, E.; Fauth, F.; Carlier, D.; Masquelier, C.; Croguennec, L. Aluminum Substitution for Vanadium in the Na 3 V 2 (PO 4) 2 F 3 and Na 3 V 2 (PO 4) 2 FO 2 Type Materials. *Chem. Commun.* **2019**, *55*

(78), 11719–11722.
(61) Zhao, L.; Zhao, H.; Du, Z.; Chen, N.; Chang, X.; Zhang, Z.; Gao, F.; Trenczek-Zajac, A.; Świerczek, K. Computational and Experimental Understanding of Al-Doped Na3V2-XAlx(PO4)3 Cathode Material for Sodium Ion Batteries: Electronic Structure, Ion Dynamics and Electrochemical Properties. *Electrochim. Acta* **2018**, *282*, 510–519.
(62) Lamsakhar, N. E. H.; Zriouil, M.; Assani, A.; Saadi, M.; El Ammari, L. Crystal Structure of Disilver(I) Dizinc(II) Iron(III) Tris-(Orthovanadate) with an Alluaudite-Type Structure. *Acta Crystallogr. Sect. E Crystallogr. Commun.* **2018**, *74*, 1155–1158.
(63) Hadouchi, M.; Assani, A.; Saadi, M.; Lahmar, A.; El Marssi, M.; El Ammari, L. Magnetic Properties of a New Cobalt Hydrogen Vanadate with a Dumortierite-like Structure: Co13.5(OH)6(H0.5VO3.5)2(VO4)6. *Acta Crystallogr. Sect. C Struct. Chem.* **2019**, *75*, 777–782.
(64) El, N.; Lamsakhar, H.; Hadouchi, M.; Zriouil, M.; Assani, A.; Saadi, M.; Lahmar, A.; Marssi, M. El; Ammari, L. El; Houda, N. El. A Novel Alluaudite-Type Vanadate, Na2Zn2Fe(VO4)3 : Synthesis, Crystal Structure, Characterization and Magnetic Properties. *Inorg. Chem. Commun.* **2019**, *107*, 107472.
(65) Hadouchi, M.; Assani, A.; Saadi, M.; Lahmar, A.; El Marssi, M.; Sajieddine, M.; El Ammari, L. Synthesis, Characterization, and Magnetic Properties of A2Co2Fe(VO4)3 (A = Ag or Na) Alluaudite-Type Vanadates. *J. Supercond. Nov. Magn.* **2019**, *32* (8), 2437–2446.
(66) Yahia, H. Ben; Shikano, M. Structural Properties of the Alluaudite-Type Materials Ag2–XNaxMn3(VO4)3 (X=0.62 and 1.85). *Zeitschrift für Naturforsch. B* **2019**, *74* (9), 677–684.
(67) Smith Pellizzeri, T. M.; Morrison, G.; McMillen, C. D.; zur Loye, H. C.; Kolis, J. W. Sodium Transition Metal Vanadates from Hydrothermal Brines: Synthesis and Characterization of NaMn4(VO4)3, Na2Mn3(VO4)3, and Na2Co3(VO4)2(OH)2. *Eur. J. Inorg. Chem.* **2020**, *2020* (35), 3408–3415.
(68) Ben Yahia, H.; Shikano, M.; Tabuchi, M.; Belharouak, I. Synthesis, Crystal Structure, and Properties of the Alluaudite-Type Vanadates Ag2-XNaxMn2Fe(VO4)3. *Inorg. Chem.* **2016**, *55* (9), 4643–4649.
(69) Middlemiss, D. S.; Ilott, A. J.; Clément, R. J.; Strobridge, F. C.; Grey, C. P. Density Functional Theory-Based Bond Pathway Decompositions of Hyperfine Shifts: Equipping Solid-State NMR to Characterize Atomic Environments in Paramagnetic Materials. *Chem. Mater.* **2013**, *25* (9), 1723–1734.
(70) Clément, R. J.; Pell, A. J.; Middlemiss, D. S.; Strobridge, F. C.; Miller, J. K.; Whittingham, M Stanley Emsley, L.; Grey, C. P.; Pintacuda, G. Spin-Transfer Pathways in Paramagnetic Lithium Transition-Metal Phosphates from Combined Broadband Isotropic Solid-State MAS NMR Spectroscopy and DFT Calculations. *J. Am. Chem. Soc.* **2012**, *134* (41), 17178–17185.
(71) Clément, R. J.; Middlemiss, D. S.; Seymour, I. D.; Ilott, A. J.; Grey, C. P. Insights into the Nature and Evolution upon Electrochemical Cycling of Planar Defects in the β-NaMnO 2 Na-Ion Battery Cathode: An NMR and First-Principles Density Functional Theory Approach. *Chem. Mater.* **2016**, *28* (22), 8228–8239.
(72) Clément, R. J.; Xu, J.; Middlemiss, D. S.; Alvarado, J.; Ma, C.; Meng, Y. S.; Grey, C. P. Direct Evidence for High Na + Mobility and High Voltage Structural Processes in P2-Na x [Li y Ni z Mn 1−y−z]O 2 (x , y , z ≤ 1) Cathodes from Solid-State NMR and DFT

Calculations. *J. Mater. Chem. A* **2017**, *5* (8), 4129–4143.
(73) Trease, N. M.; Seymour, I. D.; Radin, M. D.; Liu, H.; Liu, H.; Hy, S.; Chernova, N.; Parikh, P.; Devaraj, A.; Wiaderek, K. M.; Chupas, P. J.; Chapman, K. W.; Whittingham, ‖ M Stanley; Meng, Y. S.; Van Der Van, A.; Grey, C. P. Identifying the Distribution of Al 3+ in LiNi 0.8 Co 0.15 Al 0.05 O 2. *Chem. Mater.* **2016**, *28* (22), 8170–8180.
(74) Kim, J.; Middlemiss, D. S.; Chernova, N. A.; Zhu, B. Y. X.; Masquelier, C.; Grey, C. P. Linking Local Environments and Hyperfine Shifts: A Combined Experimental and Theoretical 31 P and 7 Li Solid-State NMR Study of Paramagnetic Fe(III) Phosphates. *J. Am. Chem. Soc.* **2010**, *132* (47), 16825–16840.
(75) Lee, Y.; Woo, A. J.; Han, K. S.; Ryu, K. S.; Sohn, D.; Kim, D.; Lee, H. Solid-State NMR Studies of Al-Doped and Al2O3-Coated LiCoO2. *Electrochim. Acta* **2004**, *50* (2–3), 491–494.
(76) Haouas, M.; Taulelle, F.; Martineau, C. Recent Advances in Application of 27Al NMR Spectroscopy to Materials Science. *Prog. Nucl. Magn. Reson. Spectrosc.* **2016**, *94–95*, 11–36.
(77) Chalmin, E.; Farges, F.; Brown, G. E. A Pre-Edge Analysis of Mn K-Edge XANES Spectra to Help Determine the Speciation of Manganese in Minerals and Glasses. *Contrib. to Mineral. Petrol.* **2009**, *157* (1), 111–126.
(78) Goodenough, J. B. Theory of the Role of Covalence in the Perovskite-Type Manganites [La, M(II)]MnO3. *Phys. Rev.* **1955**, *100* (2), 564.
(79) Goodenough, J. B. An Interpretation of the Magnetic Properties of the Perovskite-Type Mixed Crystals La1−xSrxCoO3−λ. *J. Phys. Chem. Solids* **1958**, *6* (2–3), 287–297.
(80) Kanamori, J. Superexchange Interaction and Symmetry Properties of Electron Orbitals. *J. Phys. Chem. Solids* **1959**, *10* (2–3), 87–98.
(81) Padhi, A. K.; Nanjundaswamy, K. S.; Goodenough, J. B. Phospho-olivines as Positive-Electrode Materials for Rechargeable Lithium Batteries. *J. Electrochem. Soc.* **1997**, *144* (4), 1188.
(82) Padhi, A. K.; Nanjundaswamy, K. S.; Masquelier, C.; Goodenough, J. B. Mapping of Transition Metal Redox Energies in Phosphates with NASICON Structure by Lithium Intercalation. *J. Electrochem. Soc* **1997**, *144* (8), 2581.
(83) Chen, H.; Wong, L. L.; Adams, S. SoftBV – a Software Tool for Screening the Materials Genome of Inorganic Fast Ion Conductors. *Acta Crystallogr. Sect. B Struct. Sci. Cryst. Eng. Mater.* **2019**, *75* (1), 18–33.
(84) Essehli, R.; Ben Yahia, H.; Amin, R.; El-Mellouhi, F.; Belharouak, I. Selective Sodium-Ion Diffusion Channels in Na2-XFe3(PO4)3 Positive Electrode for Na-Ion Batteries. *Energy Storage Mater.* **2020**, *24*, 343–350.
(85) Oyama, G.; Pecher, O.; Griffith, K. J.; Nishimura, S. I.; Pigliapochi, R.; Grey, C. P.; Yamada, A. Sodium Intercalation Mechanism of 3.8 v Class Alluaudite Sodium Iron Sulfate. *Chem. Mater.* **2016**, *28* (15), 5321–5328.
(86) Coelho, A. A. TOPAS and TOPAS-Academic: An Optimization Program Integrating Computer Algebra and Crystallographic Objects Written in C++. *J. Appl. Crystallogr.* **2018**, *51* (1), 210–218.
(87) Momma, K.; Izumi, F. VESTA: A Three-Dimensional Visualization System for Electronic and Structural Analysis. *J. Appl. Crystallogr.* **2008**, *41* (3), 653–658.
(88) Massiot, D.; Fayon, F.; Capron, M.; King, I.; Le Calvé, S.; Alonso, B.; Durand, J. O.; Bujoli, B.; Gan, Z.; Hoatson, G. Modelling One- and Two-Dimensional Solid-State NMR

Spectra. *Magn. Reson. Chem.* **2002**, *40* (1), 70–76.
(89) Ravel, B.; Newville, M. ATHENA, ARTEMIS, HEPHAESTUS: Data Analysis for X-Ray Absorption Spectroscopy Using IFEFFIT. *J. Synchrotron Radiat.* **2005**, *12* (4), 537–541.
(90) Dovesi, R.; Saunders, V. R.; Roetti, C.; Orlando, R.; Zicovich-Wilson, C. M.; Pascale, F.; Civalleri, B.; Doll, K.; Harrison, N. M.; Bush, I. J. *, Y. Noël, L. Maschio, A. Erba, M. Rerat and S. Casassa*; 2017.
(91) Dovesi, R.; Erba, A.; Orlando, R.; Zicovich-Wilson, C. M.; Civalleri, B.; Maschio, L.; Rérat, M.; Casassa, S.; Baima, J.; Salustro, S.; Kirtman, B. Quantum-Mechanical Condensed Matter Simulations with CRYSTAL Electronic Structure Theory Density Functional Theory. *Wiley Interdiscip. Rev. Comput. Mol. Sci.* **2018**, *8* (4), 1360.
(92) Ong, S. P.; Richards, W. D.; Jain, A.; Hautier, G.; Kocher, M.; Cholia, S.; Gunter, D.; Chevrier, V. L.; Persson, K. A.; Ceder, G. Python Materials Genomics (Pymatgen): A Robust, Open-Source Python Library for Materials Analysis. *Comput. Mater. Sci.* **2013**, *68*, 314–319.
(93) Vosko, S. H.; Wilk, L.; Nusair, M. Accurate Spin-Dependent Electron Liquid Correlation Energies for Local Spin Density Calculations: A Critical Analysis. *Can. J. Phys.* **1980**, *58* (8), 1200–1211.
(94) Lee, C.; Yang, W.; Parr, R. G. Development of the Colle-Salvetti Correlation-Energy Formula into a Functional of the Electron Density. *Phys. Rev. B* **1988**, *37* (2), 785.
(95) Becke, A. D. A New Mixing of Hartree--Fock and Local Density-Functional Theories. *J. Chem. Phys* **1993**, *98*, 1372.
(96) Stephens, P. J.; Devlin, F. J.; Chabalowski, C. F.; Frisch, M. J. Ab Initio Calculation of Vibrational Absorption and Circular Dichroism Spectra Using Density Functional Force Fields. *J. Phys. Chem.* **1994**, *98* (45), 58.
(97) Cora, F, M. Alfredsson, G. Mallia, DS Middlemiss, WC Mackrodt, R. D. and R. O. *Principles and Applications of Density Functional Theory in Inorganic Chemistry II*, 12th ed.; Springer: Berlin, Heidelberg, 2004.
(98) Muscat, J.; Wander, A.; Harrison, N. M. On the Prediction of Band Gaps from Hybrid Functional Theory. *Chem. Phys. Lett.* **2001**, *342* (3–4), 397–401.
(99) Rio De, I.; Moreira, P. R.; Illas, F.; Martin, R. L. Effect of Fock Exchange on the Electronic Structure and Magnetic Coupling in NiO. *Phys. Rev. B* **2002**, *65* (15), 155102.
(100) Middlemiss, D. S.; Lawton, L. M.; Wilson, C. C. A Solid-State Hybrid Density Functional Theory Study of Prussian Blue Analogues and Related Chlorides at Pressure. *J. Phys. Condens. Matter* **2008**, *20* (33), 335231.
(101) Feng, X.; Harrison, N. M. Magnetic Coupling Constants from a Hybrid Density Functional with 35% Hartree-Fock Exchange. *Phys. Rev. B* **2004**, *70* (9), 092402.
(102) Schäfer, A.; Horn, H.; Ahlrichs, R. Fully Optimized Contracted Gaussian Basis Sets for Atoms Li to Kr. *J. Chem. Phys.* **1998**, *97* (4), 2571.
(103) Monkhorst, H. J.; Pack, J. D. Special Points for Brillouin-Zone Integrations. *Phys. Rev. B* **1976**, *13*.

TOC Graphic

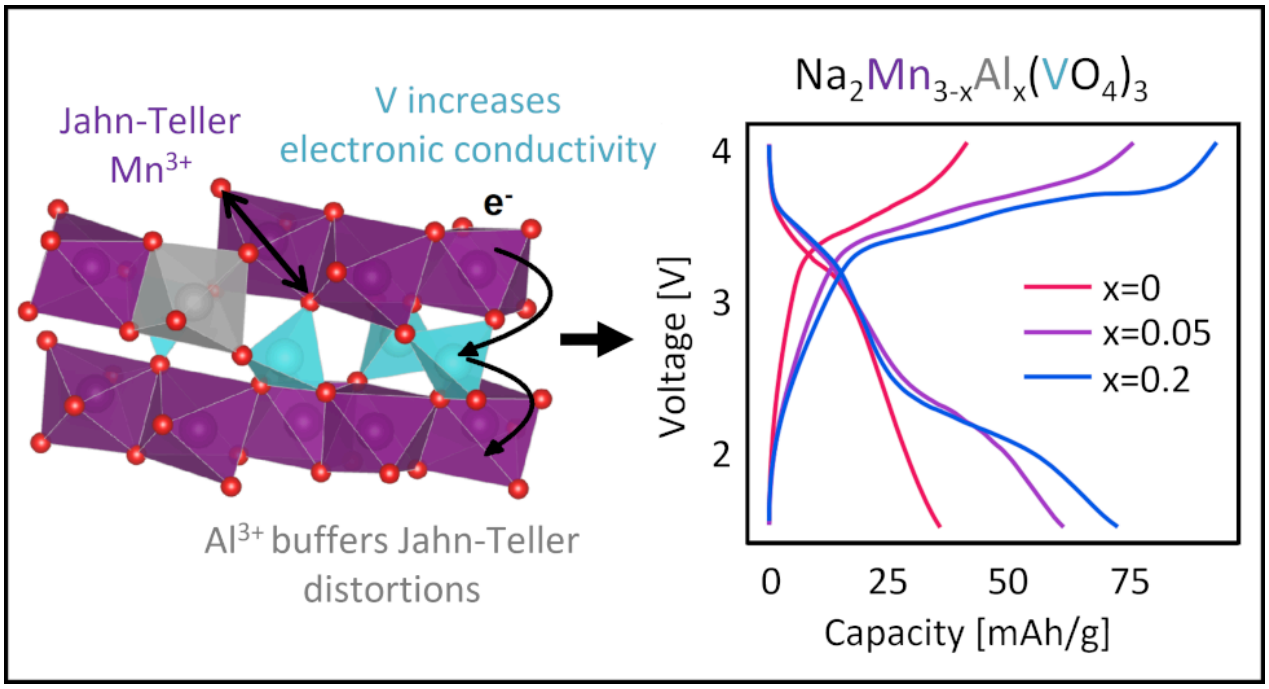
Jahn-Teller
Mn3+
V increases
electronic conductivity
e-
Al3+ buffers Jahn-Teller
distortions
Na2Mn3-xAlx(VO4)3
Voltage [V]
4
3
2
0
25
50
75
Capacity [mAh/g]
x=0
x=0.05
x=0.2